8-2019

Parametric Study of Mixture Component Contributions to Compressive Strength and Impact Energy Absorption Capacity of a High Strength Cementitious Mix with no Coarse Aggregate

Md. Abdullah Al Sarfin
Utah State University

PARAMETRIC STUDY OF MIXTURE COMPONENT CONTRIBUTIONS TO COMPRESSIVE STRENGTH AND IMPACT ENERGY ABSORPTION CAPACITY OF A HIGH STRENGTH CEMENTITIOUS MIX WITH NO COARSE AGGREGATE

By

Md. Abdullah Al Sarfin

A thesis submitted in partial fulfillment
of the requirements for the degree

of

MASTER OF SCIENCE

in

Civil and Environmental Engineering

Department of Civil and Environmental Engineering

Approved:

_____	_____
Andrew Sorensen, Ph.D. Major Professor	Marc Maguire, Ph.D. Committee Member
_____	_____
Angela Minichiello, Ph.D., P.E. Committee Member	Richard S. Inouye, Ph.D. Vice Provost for Graduate Studies

UTAH STATE UNIVERSITY
Logan, Utah

2019

ABSTRACT

PARAMETRIC STUDY OF MIXTURE COMPONENT CONTRIBUTIONS TO COMPRESSIVE STRENGTH AND IMPACT ENERGY ABSORPTION CAPACITY OF A HIGH STRENGTH CEMENTITIOUS MIX WITH NO COARSE AGGREGATE

by

Md. Abdullah Al Sarfin, Master of Science

Utah State University, 2019

Major Professor: Dr. Andrew Sorensen
Department: Civil and Environmental Engineering

The search for the next innovative, novel, cement based material in concrete technology has produced several high strength and high performance materials in past thirty years, such as High Strength Concrete (HSC), Fiber Reinforced Concrete (FRC), Ultra High Performance Concrete (UHPC), and Ultra High Performance Fiber Reinforced Concrete (UHPFRC). This research aims to contribute to this trend and produce a less expensive, cement based High Strength Concrete Mix (HSCM). The HSCM mix described in this thesis is based on the method of producing UHPC-improvement of homogeneity by replacing coarse and fine aggregates with fine sands, increased dry-compacted density of the paste by utilizing superplasticizer, silica fume, low water cement ratio, and improvement of microstructure by applying heat during curing process. The mix design is altered to evaluate the contribution of different components to compressive strength and impact energy absorption capacity.

Compressive testing at four different strain rates, in addition to the ASTM standard compressive strength test, are considered to determine the mixture components' contribution to compressive strength. These strain rates represent strain rate regimes ranging from quasi-static to the strain rates observed during soft vehicular impact and earthquakes. Impact energy absorption capacity is determined using a modified Charpy impact test. ASTM standards are followed for testing and mixing procedure where possible and necessary adjustment of the standards are made as required. Trends observed from parametric study is reported as well as relationships among compressive strength, compressive toughness, and impact toughness are proposed. This research demonstrates that it is possible to predict the impact toughness of HSCM specimens from compressive strength and toughness.

(115 pages)

PUBLIC ABSTRACT

PARAMETRIC STUDY OF MIXTURE COMPONENT CONTRIBUTIONS TO COMPRESSIVE STRENGTH AND IMPACT ENERGY ABSORPTION CAPACITY OF A HIGH STRENGTH CEMENTITIOUS MIX WITH NO COARSE AGGREGATE

Md. Abdullah Al Sarfin

This research project has been undertaken to produce and characterize the behavior of High Strength Cementitious Mix (HSCM), which has considerably higher compressive strength compared to conventional concrete. Components of HSCM are cement, silica fume, sand, water, and high range water reducer. The material is tested for compressive strength and impact energy absorption capacity while the amount of above mentioned components are varied parametrically. The effect of these parameters are extensively studied and trends are reported. Finally, this research projects attempts to find correlations among compressive strength, compressive toughness, and impact toughness. Limitations of the experimental program are discussed and future direction for improvement and expansion of the research program is suggested.

ACKNOWLEDGMENTS

I would like to express my sincerest gratitude to me advisor, Dr. Andrew Sorensen, for his continuous guidance, encouragement, and support throughout my graduate studies. It is a privilege to work under his supervision. I would also like to thank Dr. Robert Thomas for his valuable time, guidance, and contribution throughout this research project. I am extremely thankful to my committee members Dr. Marc Maguire and Dr. Angela Minichiello their time and contributions. I gratefully acknowledge the contribution of the faculty members, staffs, laboratory managers, fellow graduate students and lab mates, especially Fray Pozo. Additional gratitude goes to the numerous teachers, friends, and colleagues to inspired my throughout my academic career. Finally, I would like to thank my parents, siblings, and my wife, Farah Nusrat, for supporting me unconditionally to become the person and student I am today.

CONTENTS

Page

LIST OF TABLES

LIST OF FIGURES

Figure Page

LIST OF SYMBOLS AND NOTATION

C_u	Coefficient of Uniformity
D_x	Diameter of the particles for which x% of the particles are finer
d_{notch}	Notch Depth
$\dot{\varepsilon}$	Strain Rate
E_{comp}	Compressive Toughness
E_{impact}	Normalized Impact Energy absorbed
E_o	Impact Energy Absorbed
f_c'	28-days Compressive Strength
t	Thickness of the Specimen
w	Width of the Specimen

CHAPTER 1

INTRODUCTION

1.1 General Background

Concrete is one of the most widely used materials in construction. It has been used in large scale since the Roman ages. Up until 1990s, the compressive strength of Portland Cement Concrete typically fell in the range of 4-8 ksi for normal strength concrete and 8-12 ksi for high strength concrete. Since then, a new cementitious material has been under development in laboratory, initially by the contribution of European researchers, which reached a compressive strength of around and over 20 ksi (de Larrard and Sedran, 1994; Richard and Cheyrezy, 1995, 1994; Rossi, 2002). This new class of material is aptly named Ultra High Performance Concrete, or UHPC. Different types of fibers can be added to UHPC mix in order to imsprove brittle behavior and is identified as Ultra High Performance Fiber Reinforced Concrete (UHPFRC). In the late 1990s, commercially available UHPC mixes hit the market of Europe. In 2000, UHPC became commercially available in USA. In 2006, Mars Hill Bridge, Iowa became the first structure in USA to utilize UHPC as a construction material (Terry Wipf et al., 2011). According to US Department of Transportation website, by 2018 around 200 bridges have been built in USA with UHPC (FHWA, 2018). The promise of very high strength, excellent mechanical properties and durability has made UHPC a superior alternative to conventional concrete.

It should be noted that no precise definition of UHPC or UPHFRC can be found in literatures. But there is a common understanding that this material should have an

ultra-high compressive strength, direct tensile strength in range of 1000 to 1150 psi, very low water-binder ratio, and excellent durability (chloride penetration resistance, good freeze-thaw performance, abrasion resistance etc.) (Eide and Hisdal, 2012; Graybeal, 2006). ASTM C1856 / C1856M - 17, Standard Practice for Fabricating and Testing Specimens of Ultra-High Performance Concrete defines UHPC as the cementitious material with a compressive strength of at least 17,000 psi, with a nominal maximum aggregate size of ¼ inch, and a flow between 8 to 10 inch.

Parallel to the development of UHPC, terrorist attacks have created the need for improved blast and impact resistant construction materials. UHPC has superior compressive, tensile and flexural strength in addition to other beneficial properties like enhanced durability, negligible chloride ion penetration, improved abrasion resistance, and high resistance to freeze-thaw when compared to conventional (Alkaysi et al., 2016; Graybeal and Tanesi, 2007). These properties have made UHPC an exciting alternative to conventional concrete in extraordinary structures as well as structures that can be subjected to blast or impact and seismic loading. However, even though the compressive strength of UHPC is quite high, the direct tensile strength and high frequency shear strength is much lower than expected and must be overcome to fully utilize it in hardened structures. As such is it of worth to try and identify those factors within the UHPC that can be modified to increase the direct tensile strength.

Most of the UHPC and UHPFRC mixtures used in the construction industry in the United States are proprietary. Because these mixes are proprietary, there is a huge gap in understanding the effect of their constituents and the special treatments required to

achieve the impressively high strength, owing to the fact that the constituents' contributions in these proprietary mixes are not readily available in literature. Also, almost all the commercial mixes available incorporate fibers which provides additional strength and ductility. This research program is designed to investigate the development, characterization, and behavior of a High Strength Concrete Material (HSCM) with the final goal of developing a non-proprietary UHPC mix with and without fiber. As an extension of the study, the thesis is also focused on investigating the material's behavior under high frequency shear loading that a structural member may experience under high strain rate loading.

1.2 Problem Statement and Scope

As discussed in the previous section, UHPC has very high promise of being used in structures subjected to high intensity dynamic loading (e.g. blast and impact). Research has been conducted to understand its performance in such scenarios and it has been reported that the mechanical behavior of UHPC is highly subject to strain rates; implying the necessity to fully characterize its dynamic behavior (Othman et al., 2019; Pyo et al., 2015; Thomas and Sorensen, 2017). This research program presented in this document is designed to classify the contribution of different components of the HSCM material in its compressive strength, response to high strain rate loading, and dynamic shear absorption capacity.

The thesis aims to answer the following questions to better understand the material so that successful implementation of the material in structural application is possible:

1. Can an optimum mix design be achieved with locally available materials that meets the requirements of HSCM? How different components of the material affect the compressive strength of HSCM?
2. Can a relationship between the compressive strength, compressive toughness and impact toughness be modelled? Is it possible to predict the impact toughness of the material from the mix design and compressive strength?

1.3 Research Objective

To answer the questions stated in previous section, the objective of this research project can be summarized in two parts. The first part studies HSCM mixes with constant paste volume where different components of the material varied. The objectives are as followed:

1. Establish mixing procedure and curing method to produce a product that meet the criteria of UHPC. Several batches of HSCM mixes are to be prepared to find suitable one.
2. Test HSCM specimens for compressive strength with constant paste volume at different strain rates to determine the effect of dynamic loading.
3. Test the above mentioned HSCM batches to study the dynamic shear energy absorption capacity of the material.
4. Establish a relationship between impact toughness and compressive strength for HSCM mixes with constant paste volume.

The next phase of the experimental investigation aims to determine the effect of sand particle size, gradation, and fraction on compressive strength and energy absorption capacity. The objectives can be summarized as:

1. Investigate the effect of sand fractions, sand gradation, and maximum particle size of quartz and silica sands on HSCM compressive strength.
2. Suggest relationships between compressive strength or compressive toughness and impact toughness of the material.
3. Suggest an optimum sand fraction to improve on dynamic shear energy absorption capacity.

1.4 Research Objective

The organization of this thesis contains five chapters. The first chapter gives the general background, motivation, scopes and objective of research program. Chapter 2 contains an overview of relevant research works. In this chapter the development of UHPC, research on the mechanical properties of this material, strain rate sensitivity, structural performance and effect of impact and blast loading on conventional concrete, high strength concrete, ultra-high performance concrete, and ultra-high performance fiber reinforced concrete are discussed. The third chapter covers the methodology used to carry out the study presented in this thesis. This includes the mix design, specimen preparation, mixing and curing procedure, test methods, and experimental setups. The fourth chapter presents the experimental results obtained from laboratory tests for mixes with constant paste volume. It also explains the results and trends observed. Based on the

shortcomings observed from initial testing, the later part of this chapter is focused on the experimental investigation of the material with different sand fraction and particle size. The fifth and final chapter draws conclusions from this research and discusses future work of this topic. The developed mix proportion, material specifications, detailed measurement of test specimens, and raw test results of individual specimens are included in the appendices.

CHAPTER 2

LITERATURE REVIEW

This chapter presents a review of the literature relevant to the study ultra-high performance concrete (UHPC). The chapter is divided into six sections. The first section presents the historical development of UHPC. The second section discusses the mechanical properties of UHPC, investigated by different researchers over the years. The third section presents a discussion of the strain rate sensitivity of UHPC. The fourth section is dedicated to the structural performance of UHPC. The fifth section discusses performance of UHPC under blast and impact load. The sixth and last section summarizes the literature review relevant to the current research program.

2.1 Historical Development of UHPC

For nearly five decades, significant development and understanding in cementitious matrix and fiber reinforcement has been achieved. The effect of fine sand, development of admixtures, and studies on the bond between fiber and cementitious matrix have led to high performance and ultra-high performance cementitious materials. There are quite a few number of variants of UHPC developed since the mid-1990s. In 1990s, European researchers were at the forefront of the development and material testing of UHPC. Though since early 2000s, researchers in the United States have been extensively researching on this novel material.

In 1994, Reactive Powder Concrete (RPC), one of the earliest variants of UHPC, was introduced (Richard and Cheyrezy, 1994). The researchers presented the composition

of two types of RPC: RPC 200 and RPC 800, and their possible application in structures and structural components. The underlying research principles of their research program were to eliminate coarse aggregates to enhance homogeneity, optimization of granular mixture to enhance compacted density, application of pressure before and during setting, post-set heat curing to enhance microstructure, incorporation of small sized steel fibers to improve ductility, using low water-cement ratio and higher optimum superplasticizer ratio, addition of steel fibers to improve ductility, and maintaining mixing and casting procedure as close as possible to industry practice. The authors envisioned the use of RPC 200, the production and application of which are close to that of conventional concrete, for structures not incorporating traditional passive reinforcement due to its high ductility. Elimination of reinforcement, reduction of permanent loads by lightening the structure, and reduction of the quantities of concrete used can save significant cost. The possible use of RPC 800 would be in manufacturing mechanical parts in place of steel, hardening military structures or equipment, and in nuclear and industrial waste storage facilities due to its excellent projectile impact resistance and ultra-dense microstructure.

de Larrard and Sedran (1994) proposed the optimization of UHPC by the use of a packing model. The researchers aimed to see which strength level can be obtained by using normal, untreated aggregates, Portland cement, silica fume, and superplasticizer with the help of thermal curing. The considerations on the parameters to be optimized during the mix design process were also presented. Based on fluid consistency, classical components, and moderate thermal curing, an optimum material was sought. With the help of Solid Suspension Modelling (SSM), a selection of mixes was made and tested to

verify the optimality of the mix. The authors reported the production of a fluid mortar with water/binder ratio of 0.14 and a compressive strength of 34 ksi (236 MPa) (de Larrard and Sedran, 1994).

Thanks to the extensive research, Lafarge introduced DUCTAL®; a commercially available proprietary fiber reinforced UHPC material in the mid 1990's (Chanvillard, Pimienta, Pineaud, & Rivillon, 1996). The material is reported to reach 29 ksi (200 MPa) with the help of heat curing at 90°C for 3 days, and steel fiber content up to 6%. In 2002, Rossi et al. developed CEMTEC$_{multiscale}$® with fiber content up to 9%, achieving compressive strength up to 29 ksi (200 MPa) (Rossi, 2002). Since the beginning of 2000s, researcher around the globe invented different types of UHPC and UHPFRC mainly based on DUCTAL® and CEMTEC$_{multiscale}$®.

In 1999, a microstructural investigation of hardened mixes of UHPC mixtures with incorporated micro carbon fibers was carried out to better understand and enhance the mechanism of mechanical and durability performance (Reda et al., 1999). Microstructural investigation was performed by two methods: Scanning Electron Microscope (SEM) and X-Ray Diffraction (XRD). SEM micrography showed a very dense microstructure compared to that of conventional Portland cement concrete and HPC. Calcined bauxite aggregate group showed more homogenous and denser microstructures than the limestone aggregate specimens as well as excellent mechanical performance. The authors reported that the dense microstructure of the cement phase in these groups extended to the aggregate boundary and as a result microstructure gradient of the cement paste toward the transition zone was absent. The absence or reduced

thickness of transition zone was interpreted as well-developed bond between cement paste and aggregate surface. The mixtures with both silica fume and silica flour generally showed a very dense and homogeneous microstructure. The micro carbon fiber was observed to be randomly distributed. The authors also noted the general absence of large CH crystals when investigate by XRD. The authors concluded that the low water w/c ratio, ingredients used, and elevated temperature during curing created an environment that consumed most of the CH crystals and converted them to strong C-S-H. Compared to conventional concrete and HPC, the transition zone in UHPC was very small in thickness. The micro-cracks in the vicinity of the aggregate particles were also observed to be very small. Also, no additional transition zone was observed near micro carbon fibers. The bond between the paste and fibers were very dense and homogenous. The authors observed an unidentified microstructure near the fiber-paste interface with gel-like appearance which was amorphous in nature. Under SEM, the micro carbon fiber showed non smooth surface which resulted in better bond with cement paste. Little anchorage provided by the short length of fibers allowed high compressive stress and flexure toughness of the matrix but reduced strain capacity.

In 2012, Willie et al. developed UHPFRCs without any special heat treatment using commercially available materials on the U.S. market. By optimizing the packing density of the cementitious matrix, using very high strength steel fibers, tailoring the geometry of the fibers, and optimizing the matrix-fiber interface properties, enhanced performance was accomplished. It was shown that addition of 1.5% deformed fibers by volume results in a direct tensile strength of 1.9 ksi (13 MPa), which is 60% higher than

comparable UHPFRC with smooth steel fibers had a tensile strain at peak stress of 0.6%, which is about three times that for UHPFRC with smooth fibers. Researchers obtained compressive strength up to 42 ksi (292 MPa), tensile strength up to 5.4 ksi (37 MPa) and strain at peak stress up to 1.1% after 28 days curing by using up to 8% volume fraction of high strength steel fibers and infiltrating them with the UHPC matrix (Wille et al., 2012).

Recently, researchers are performing tests to evaluate the behavior of UHPC under varying strain rate, to achieve ductile behavior, behavior under dynamic and impact loads, and possible application of UHPC and UHPFRC in structural systems (Ichikawa et al. 2016; Li et al., 2015; b; Sovják et al., 2013; Yoo et al., 2014; Zhang et al., 2016; Zohrevand and Mirmiran, 2011). It should be noted that, in most of the cases, the high strength achieved are in laboratory condition and with the use of costly, high quality materials. For widespread implementation of UHPC in structural system, cost and construction techniques are among the hurdles that have yet to be overcome.

2.2 Mechanical Properties of UHPC

This section describes researches conducted over the years to characterize the mechanical properties of UHPC and UHPFRC materials through various laboratory tests. These tests include compressive strength test, measurement of fracture energy, first cracking strength, tensile strength, secant modulus, elastic modulus etc.

The RPC developed by Richard et al. has a compressive strength and fracture energy ranging from 29 ksi to 116 ksi (200MPa to 800 MPa) and 0.57 ft-lb/in^2 to 19 ft-lb/in^2 (1200 to 40,000 J/m^2). The ductility, reported in terms of fracture energy, is increased by one to two order of magnitude compared to conventional concrete. Fracture

energy is evaluated by performing three-point bending tests on notched samples. The authors report a flexural strength of 4 ksi (28 MPa) and a fracture energy 0.024 ft-lb/in^2 (50 J/m^2). Steel microfibers can result in strength ranging from 7.25 ksi to 14.8 ksi (50 to 102 MPa) and fracture energy ranging from 4.76 ft-lb/in^2 to 19 ft-lb/in^2 (10, 000 J/m^2 to 40, 000 J/m^2). This signifies very ductile behavior. The research conducted by the authors resulted in two products: RPC 200 and RPC 800. RPC 200 is developed by using Type V OPC, fine quartz sand and straight smooth steel fibers. The mixing and casting procedure is similar to those of conventional concrete. The lower value of compressive strength is 24.7 ksi (170 MPa) at 28 days of curing at ambient temperature. When the specimens are heat-cured at 80-90℃ after two days of curing at ambient temperature, upper value of compressive strength is achieved, which is 33.4 ksi (230 MPa). The authors reported that the flexural strength and flexural energy are variable with the percentage of fibers added. In tests, RPC 200 shows great strain hardening followed by gradual strain softening. The first cracking strength of RPC 200 is two times that of conventional concrete. Authors reported about ten times greater displacement at maximum stress than that at the first crack. RPC 800 can be cast using the same components of RPC 200 except by using stainless steel microfiber instead of steel fibers. The dry curing temperature of equal or greater than 250℃ is applied after demolding. Before and after setting, pressure has to be applied in the mold to obtain improved properties. Compressive strength and fracture energy achieved are more than ten times than those of conventional concrete. 116 ksi (800 MPa) strength can be achieved by using steel powder instead of quartz sand. The

Young's modulus of RPC exceeds 7252 ksi (50 GPa) and can be as high as 10878 ksi (75 GPa) (Richard and Cheyrezy, 1995).

Hebel et al. (2006) studied hydration kinetics of self-compacting UHPFRC ($CEMTEC_{multiscale}$®) by using semi-adiabatic heat of hydration tests. One of the objective was to verify whether the models for conventional concrete are in agreement with the results obtained for UHPFRC. For UHPFRC, the rate of development of mechanical properties was highs for secant modulus, followed by the compressive and then tensile strength. Secant modulus were determined at 30% of the compressive strength of cylindrical specimens. Compressive strength test results showed significant strain hardening. The strain at the ultimate tensile strength as well as the secant modulus at the beginning of the test were determined for each specimen. Using extended Powers' model for a closed system, the theoretical total degree of hydration was investigated. The cement and silica fume final degrees of hydration were determined separately with the Waller model. Based on the results from the two models, the final degree of hydration of the silica fume and cement for the studied UHPFRC was assessed to be α=0.31. The study found that the hydration reaction started at 26 hours after the addition of water and was retarded due to high amount of superplasticizer added. The authors described the reaction rate a function of the degree of reaction with a power-type model, which is used for conventional concrete. It is found that the mechanical properties started to develop at degree of reaction 0.16 at approximately 32 hours after addition of water. After 90 days, the degree of reaction amounted to 0.99. This indicated the completion of hydration reaction after 90 days and the material became inert beyond this age. The author

concluded that the development of compressive properties and the secant moduli is faster than compared to tensile properties (Habel et al., 2006).

In 2015, Yoo and Yoon investigated UHPC beams with steel reinforcement for structural performance. Two reinforcement ratios and smooth and twisted fiber reinforcement were used for the specimens. For smooth steel fibers (S), 0.5, 0.77, and 1.18 inch (13, 19.5 and 30mm) fiber lengths were used. 1.18 inch (30 mm) long steel fibers were selected for the twisted fibers (T). The tests showed that the specimens with steel fibers had a slightly higher compressive strength and elastic modulus compared to the specimens without fibers. Elastic modulus was reported not to vary with respect to fiber length and type. Linear stress-strain curve up to failure was reported. The failure was in brittle manner. The authors reported significant improvement of flexural performance (strength, deflection capacity and CMOD at peak). T30 specimens had the highest flexural strength. The deflection capacity of T30 specimens were reported to be in between S30 and S19.5. T30 specimens showed a steeper decrease in load carrying capacity after peak load compared to S30 specimens (Yoo and Yoon, 2015).

Pyo et al. (2015) reports an experimental investigation of UHPFRC uniaxial tensile response in order to obtain detailed knowledge of the tensile behavior of UHPFRC. The dog-bone specimens of 3-inch length were tested under four strain rates (0.1, 0.01, 0.001, and 0.0001 per second). Five different fiber types, including straight and twisted, were considered. The other geometric properties of the fibers that varied were: diameter, length, and tensile strength. Three fiber volume fractions (1%, 2%, and 3%) were used. For the experiments, total 108 dog-bone shaped specimens were tested.

From the experimental data, strain hardening and high energy absorption (≥ 238000 ft-lb/in^2 or 50 kJ/m^3) were observed for all loading rates. Authors reported that the post-cracking strength and the corresponding strain generally increased with an increase in both volume fraction of fiber and strain rate. When the volume fraction of fiber goes from 1% to 3%, the post-cracking strength almost doubles. The authors reported similar trend using smooth steel fibers with 1% and 2% volume content. For either smooth or twisted fibers with same aspect ratio, the post-cracking strength increased with an increase in strain rate. Both the post-cracking and first cracking strength generally increased with fiber aspect ratio. The study exhibited better performance from twisted fibers. This is attributed to the additional anchorage effect associated with the untwisting action that occur during pullout. It was also observed that, for a given volume fraction, the T-0.3-25 (twisted-0.3mm dia-25mm length or 0.0118 inch dia-1-inch length) and the S-0.2-25 (straight-0.2mm dia-25mm length or 0.0079 inch dia-1-inch length) fibers showed similar mechanical performance. This can be explained by the fact that thinner fibers have more numbers in a unit volume and thus made up for the additional anchorage mechanism of twisted fibers, although the large number of fibers is more difficult to mix. The authors reported that equivalent bond strength is almost independent of fiber type, diameter and length. The authors speculated that this unexpected result can be explained by the excellent bond of fiber in the UHPC matrix due to surface abrasion and high packing density of cementitious matrix around the fiber. The post-cracking strength increased with fiber reinforcing index ($V_f(l_f/d_f)$) and quantified with least square fit lines for all loading rates. Here, V_f, l_f, and d_f are the fiber volume fraction, length of fiber, and

diameter of fiber, respectively The author plotted the variation of the first cracking strength of the composite versus the fiber reinforcing index and found that the first cracking strength increases with the index. The plot of energy absorption capacity vs. $V_f(l^2_f/d_f)$ confirmed the theoretical prediction that energy increases with both $V_f(l^2_f/d_f)$ and strain rate. The data showed that the number of cracks and the energy absorption capacity increased with increasing fiber volume fraction. Because of the subjective nature of crack counting process and due to the variability of test data, definite conclusion was difficult to draw. The study reported that the fiber tensile stress generally decreased for higher fiber volume fraction. This is in contrast to the general trend of improved mechanical properties with increasing fiber volume fraction. The authors speculated the fiber-group effect as the mechanism behind this (Pyo et al., 2015).

2.2.1 Effect pf Size and Geometry

In 2014, Nguyen et al. reported direct tensile stress versus strain response of UHPFRC with various sizes and geometries (Nguyen et al., 2014). The specimens were prepared with twisted macro and smooth micro steel fibers. The authors reported that all series of specimens produced strain hardening behavior regardless of size or geometry of specimens. Tensile stress versus strain responses across the series were found to be different. All series generated multiple micro cracks. Across the sizes and geometries, the post cracking strength varied very little. Although, it was reported that the strain capacity at peak stress varied significantly as the size of specimens varied. The strain capacity, energy absorption capacity and the average crack spacing were found to be highly sensitive to sizes and geometries of specimens. Post cracking strength decreased slightly

as the gauge length increased. Strain capacity and energy absorption capacity decreased while and average crack spacing generally increased as the gauge length increased. As the section area of the specimens increased, post cracking strength decreased slightly, while significant decrease in strain capacity and energy absorption capacity and increase in average crack spacing were reported. Post cracking strength decreased slightly as the volume of specimens increased, while strain capacity and energy absorption capacity significantly decreased. Average crack spacing increased significantly. Post cracking strength and strain capacity slightly increased as the thickness of the specimens increased. Considerable increase in energy absorption capacity were also observed. Average crack spacing decreased noticeably. Overall, the effect of thickness on the mechanical properties of the specimens are opposite to that of gauge length, section area and volume (Nguyen et al., 2014).

2.2.2 Effect of Fiber Length and Placement Method

In 2014, Yoo et al. investigated the effect of fiber length and placement method on the mechanical properties (flexural behavior, tension-softening curve, and fiber distribution characteristics) of UHPFRC. 4×8 inch cylindrical specimens for compressive strength test and 4×4×16 inch notched specimens for three-point bending were prepared Two different placement methods were adopted: placing concrete at the center of the specimen, and placing concrete at the corner of the specimen. Experimental data showed that the compressive strength is seldom influenced by fiber length. Specimens with fiber length 0.5 and 1.18 inch (13 and 30 mm) showed about 9% higher elastic modulus than specimens with 0.64 and 0.77 inch (16.3 and 19.5 mm) fiber length. Flexural test results

showed that the initial stiffness is barely affected by fiber length. Peak flexural load increased with an increase in fiber length up to 0.77 inch (19.5 mm), while specimens with fiber length of 1.18 inch (30 mm) showed a decreasing trend. The later phenomenon was attributed to the difficulty to achieve uniformity of dispersion of fiber in the matrix and the lower number of fibers at the crack plane. Higher peak load and lower post-peak ductility was observed for specimens with concrete placed in the center. For each test series, the first cracking loads from the Limit of Proportionality (LOP) in both of the load-deflection and load crack mouth opening displacement (CMOD) were almost similar, concluding that the LOP in load-deflection and load-CMOD curves can be defined as the first cracking point for UHPFRC beams with 2% volume of smooth steel fibers. No noticeable difference for fiber length variation was observed from first crack strength and the corresponding deflection and CMOD curves were reported. Slightly higher values were achieved for the specimens with the concrete placed in the center. Increase in flexural strength, deflection and CMOD at peak load were observed with increasing fiber length up to 19.5 mm. Again, higher flexural strength was observed for specimens with concrete placed in the center. Deflection and CMOD at peak load was not significantly affected by placement method. Strength and deflection capacity deteriorated for 30 mm fibers (Yoo et al., 2014).

2.2.3 Effect of Fiber Content

Yoo et al. investigated the effect of fiber content on the mechanical properties of UHPFRC. The fiber volume fractions in the identical mortar matrix were 1%, 2%, 3%, and 4%. The authors performed inverse analysis and based on the result, presented a bi-

linear softening curve for UHPFRC. The effect of fiber volume fraction on the bond properties of steel fiber was tested with half-dog-bone shaped pullout specimens. Half of the length of the fibers was embedded into the matrix. The test results showed that the load carrying capacity and elastic modulus in compression increased with the increasing amount of fiber content up to a fiber volume of 3%. But the specimen with 4% fiber volume had the lowest compressive strength and elastic modulus. The improved compressive strength and elastic modulus is attributed to the fibers' ability to delay micro-cracking and to arrest crack propagation. The author concluded that the lowest compressive strength and elastic modulus was due to difficulty in providing a homogenous distribution of fibers in the mixtures. UHPFRC shows a very linear stress-strain curve, regardless the fiber content. The material failed in a brittle manner without significant fragmentation. Fibers in the matrix increased the bond strength of the matrix. The paper reports that average and equivalent bond strength and pullout energy improved with the increased fiber volume fraction up to 2%, then these parameters deteriorated. The specimen with 3% fiber volume exhibited lower bond strength compared to the specimen with 2% fiber volume, though having the maximum compressive strength among all the specimens. The mechanism for this is the lower confinement pressure of the matrix due to lower composite shrinkage of higher volume fraction. The flexural strength, deflection and CMOD at peak load were found to be pseudo-linearly increasing with the increase in the fiber volume fraction. This is due to the improved bridging effect with higher fiber volume fraction. The first cracking load, corresponding deflection and CMOD under flexure showed no appreciable difference due to increasing or decreasing

fiber volume. The higher amount of fiber resulted in more brittle behavior (Yoo et al., 2013).

2.3 Strain Rate Sensitivity

Mechanical properties of concrete are dependent on the strain rate of loading. Typically, the effect of strain rate is reported as a dynamic increase factor (DIF), which is the ratio of dynamic-to static strength for the same loading mechanism.

2.3.1 Strain Rate Effect on Conventional Concrete

Malvar and Ross (1998) analyzed 15 sets of data available from different researchers and provided an updated DIF-versus-strain rate relationship for concrete in tension. The data reviewed by the authors supported that the dynamic impact factor (DIF) is a bilinear function when plotted in log-log scale, with no increase for strain rate below 10^{-6} /s with a slope change at a strain rate of 1 /s. Mellinger and Brikimer (1966) tested two sets of three tests on plain concrete cylinders under impact load. The first data set represented a DIF between 5.1 and 6.5 at a strain rate about 20 /s. The second data set the reported DIF was between 4.5 and 8.1 at a strain rate 23 /s. Birkimer (1971) conducted 46 impact tests on plain concrete cylinder at a strain rate between 2 and 23 /s. The DIF from this study ranged between 2.5 to 6. Ross et al. (1995) tested cylindrical concrete specimens in a Split-Hopkinson Pressure Bas (SHPB) in direct tension, splitting tension and direct compression. The strain rate in tension ranged from about 10^{-7} to 20 /s with DIF up to 6.47 at 17.8 /s rate. John et al. (1992) tested six sets of specimens in splitting tension in Split-Hopkinson Pressure Bar with strain rate ranging from 5×10^{-7} to 70 /s. The

DIF value reached up to 4.8. Antoun (1991) performed plate impact tests to determine uniaxial strain tensile test. This is assumed to be similar to uniaxial unconfined tensile strength. The DIF value found to be in excess of 3. The author noted that all the data from the experiments above strain rate 1 /s showed the same trend. In all cases, very high dynamic tensile strengths were observed compared to quasi-static strength of concrete.

Using a bilinear CEM formulation, Malvar and Ross (1998) reported that the change in slope of DIF-strain rate curve is at 30 /s. However, the authors noted that the experimental data at high strain rates fell to the left of the theories and indicates to a change in slope in the bilinear relationship closer to 1 /s. For concrete in tension, the authors reported lack of data for low strain rate. Based on all these study, they proposed the formulation shown in equation (2.1) which assumed the quasi-static strain rate at 1×10^{-6} /s and change in slope close to 1 /s (Malvar and Ross, 1998).

$$f_t/f_{ts} = \begin{cases} \left(\dot{\varepsilon}/\dot{\varepsilon}_s\right)^{\delta}, & \dot{\varepsilon} \le 1s^{-1} \\ \beta\left(\dot{\varepsilon}/\dot{\varepsilon}_s\right)^{1/3}, & \dot{\varepsilon} > 1s^{-1} \end{cases} \qquad (2.1)$$

Where,

$\delta = 1/(1 + 8f'c/f'_{co})$ $\quad$ $\dot{\varepsilon}_s = 10^{-6}$ /s (static strain rate)

$log\beta = 6\delta - 2$ $\quad$ f_{ts} = static tensile strength at $\dot{\varepsilon}$

$f'_{co} = 10$ MPa $\quad$ f_t/f_{ts} = tensile strength DIF

$\dot{\varepsilon}_s = 10^{-6}$ /s (static strain rate)

$\dot{\varepsilon}$ = strain rate in the range of 10^{-6} to 160 /s

2.3.2 Strain Rate Effect in Fiber Reinforced Concrete

In 2016, Othman and Marzouk reported an experimental investigation to determine the effects of strain rate on compressive strength, modulus of elasticity, and flexural tensile strength under various strain rates ranging from the static to the seismic and/or impact level of fiber-reinforced cementitious composite (FRCC) matrixes (Othman and Marzouk, 2016). Three different matrices with target compressive strength ranging from 11.6 ksi to 18.9 ksi (80 to 130 MPa) were tested according to ASTM C39 / C39M Standard Test Method for Compressive Strength of Cylindrical Concrete Specimens. Strain were captured according to ASTM C469 / C469M Standard Test Method for Static Modulus of Elasticity and Poisson's Ratio of Concrete in Compression (ASTM 2014, 2016). Two matrix contained 2% straight steel fiber by volume and a control mix without fiber. The specimens were tested for six different strain rates ranging from 3×10^{-5} to 1×10^{-1}. The researchers reported that flexural tensile strength was more sensitive than both the compressive strength and elastic modulus at the same strain rate, while compressive strength, elastic modulus and the flexural tensile strength increased with an increase in strain rates. Dynamic Impact Factor (DIF) for matrices with lower strength was found to be higher for both compression and flexure tests. In both compression and flexure, strain hardening behavior was evident under high strain rates. Cracking took place in the high moment zone in quasi-static bending and drop-weight tests. The paper reported that the final fracture occurred by fiber pullout in one localized bending crack at the mid-span of specimens and, with increasing strain rate, the fracture surface became more flattened. The study found that the CEB-fib Model (2010) fits well

for specimens without the steel fiber reinforcing in both tension and compression. But it overestimates the compressive and tensile strength enhancement for the FRCC specimens with compressive strength more than 16 ksi (110 MPa). The data obtained for FRCC is much more scattered implying that improved model for FRCC with compressive strength more than 21.8 ksi (150 MPa) is required. It should be noted that direct tension test for concrete is not used in this investigation.

In 2017, Park et al. investigated the effects of matrix strength on the rate-sensitive tensile responses of strain-hardening fiber-reinforced cementitious composites (SH-FRCC) at high strain rate. Fifteen series of tensile specimens were prepared for the experimental program. There were three types of matrices (M1, M2, M3) each having 1 % by volume long hooked (LH) macro fibers and 1 % short smooth (SS) micro steel fibers. SS fibers had higher tensile strength compared to LH fibers. M1 and M2 matrices contained Type II cement while M3 contained Type I cement. M1 and M2 matrices contained fly ash, while M2 and M3 matrices contained silica fume. Only M3 matrix contained silica powder. The superplasticizer used for M1 and M2 matrices contained 25% solid content whereas the superplasticizer used for M3 matrix contained 30% solid content. The compressive strength of M1, M2 and M3 matrices are 8, 11.75, and 26 ksi (56, 81, and 180 MPa), respectively. The applied tensile strain rates were 0.000333, 0.00333, 0.0333, 30 to 60, and 70-170 /s. From the test data, authors reported that all the specimens maintained typical strain hardening behavior even at very high strain rates of up to 170/s. Authors noted that the changes in the shape of the tensile stress versus strain curves were not significant as the strain rate increased from static rate (0.000333/s) to an

intermediate seismic rate (0.0333/s). But the shape changed significantly when the strain rate was higher than 25 /s as all the matrices show enhancements above this rate. Specimens with M1 produced the highest enhancement in the strain capacity. Specimens with M3 produced the highest enhancement in the post cracking tensile strength. Between 0.000333 and 170 /s strain rates, all the specimens generated multiple micro-cracks. The study observed that the number of cracks slightly increased as the strain rate increased from static to intermediate seismic, whereas decreased at higher strain rates. The authors didn't draw any conclusion regarding this trend. But they noticed that the micro-cracks are more uniformly distributed at the specimens with M2 and M3 matrices (high strength) compared to the specimens with M1 matrix. The number of micro-cracks at higher in the specimens with M3 matrix compared to the specimens with M1 matrix at higher strain rates (Park et al., 2017).

The enhancements of post cracking strength at higher strain rate were more significant for M3 matrix. The DIF increased with the increase of matrix strength. The post cracking strength increased monotonically- gradually at first and rapidly after 25 /s. The DIF of strain capacity at high strain rate, however, was more significant for M1 than M3. The author attributed this to the wider width of the micro-cracks at high strain rates (70 and 170/s) with no clear enhancement in the number of cracks. Consequently, the DIF of energy absorption capacity at higher strain rate for M1 specimens was higher than that of M3. The energy absorption capacity significantly increased as the strain rate increased. Overall, the tensile parameters generally increased with the strain rate, though the DIFs of tensile parameters were different across the strength of the matrix. The M3

matrix in this study contained glass powders. As the strain rate increased from 30-60/s to 70-170/s the number of non-straightened hooked steel fibers also increased, significantly for M1, but decreased slightly for other two matrices. This produced lower post cracking tensile strength because the non-straightened hooked fibers could not fully activate their mechanical pullout resistance and thus lost their resistance prematurely. Blending hooked and smooth fibers produced a noticeable enhancement in strain capacity at high strain rate because the SS fibers reduced the interfacial damage surrounding the LH fibers (Park et al., 2017).

The authors noted the limitations of the existing models such as CEB-FIB and Malvar models for predicting the DIFs of the post cracking tensile strength of SH-FRCCs as these models are based on normal concrete in tension and on linear fracture mechanism. The Park et al. model is also not sufficient as it is based on test results for UHPFRCs with matrix strength of 26.1 ksi (180 MPa). So, the authors proposed the following equation (Park et al., 2017):

$$DIFpc = \begin{cases} \left(\dot{\varepsilon}/\dot{\varepsilon}_s\right)^{\delta}, & \dot{\varepsilon} \le 25s^{-1} \\ \beta\left(\dot{\varepsilon}/\dot{\varepsilon}_s\right)^{\eta}, & \dot{\varepsilon} > 25s^{-1} \end{cases} \qquad (2.2)$$

Where,

$\delta = 0.017 - 2722 \times \left(\frac{f_c}{f_{cmo}}\right)^{-7.33}$

f_c = *Compressive strength of the matrix*

$\log \beta = -0.007082 \times - 2.08 f_c$

$f_{cmo} = 10\ MPa$ $\qquad\qquad$ $\eta = 0.1208 \times f_c^{0.2622}$

2.3.3 Strain Rate Effect on UHPC and UHPFRC

In 2009 Millon et al. investigated fiber reinforced UHPC under tensile loads at a strain rate up to 160 /s for static and dynamic material parameters and fracture behavior. A moderate 4% increase of dynamic Young's modulus of fiber reinforced UHPC was found compared to high performance concrete, which increases 35% compared to conventional concrete. Similar increase in results were obtained for static Young's modulus, while no rate dependency was reported. Compared to HPC, a strong increase in the dynamic tensile strength of fiber-reinforced UHPC was observed, where the tensile strength of UHPC increased more than by a factor of 2. Due to strain rate about 120 /s, a significant strengthening effect was reported, which led to a DIF around 5. For conventional concrete same rate effect occurred. Low strain rate effects for UHPC compared to HPC and conventional concrete was reported. Experimental results showed that the dynamic tensile strength and fracture energy increased by a factor of 3 and 29 for UHPC compared to conventional concrete (Millon et al., 2009).

Thomas and Sorensen (2017) investigated the effect of strain rate on the mechanical responses of UHPC in tension reports in a number of recent studies. The review paper concluded that the existing models underestimate the strain rate sensitivity of the tensile properties at high strength rates (Thomas and Sorensen, 2017).

The paper concluded that while the strain rate sensitivity of the tensile properties of UHPC is similar to that of conventional concrete at quasi-static and intermediate strain rates, UHPC is much more strain rate-sensitive than conventional concretes at high strain rates. The authors summarize eleven studies that reported ultimate tensile strength for

UHPC at strength rates ranges from 10^{-6} to 10^{2}. Based on the data from these literatures, the author proposed the improved model DIF for ultimate tensile strength of UHPCas given by equation (2.3) (Thomas and Sorensen, 2017).

$$DIF_{ft} = \begin{cases} \left(\dot{\varepsilon}/\dot{\varepsilon}_s\right)^{\delta}, & \dot{\varepsilon} \le 10s^{-1} \\ \beta\left(\dot{\varepsilon}/\dot{\varepsilon}_s\right)^{3/4}, & \dot{\varepsilon} > 10s^{-1} \end{cases} \qquad (2.3)$$

Where, $log\beta = 7\delta - 5.22$ *and* $\delta = 1/121$.

The authors concluded that the strain rate sensitivity of UHPC is independent of fiber volume, fiber geometry, fiber factor, or compressive strength.

Data from five studies shows that the DIF for the first cracking strength of UHPC are well described by the existing relationships of DIF for tensile strength of conventional concrete. Two studies describe the strain rate effects on the flexural strength or the modulus of elasticity of UHPC. Based on the data presented in these papers, Thomas and Sorensen (2017) propose an improved model given by Eq. (2.4) (Thomas and Sorensen, 2017).

$$\mathrm{DIF_{MOR}} = \begin{cases} \left(\dot{\varepsilon}/\dot{\varepsilon}_s\right)^{1/121}, & \dot{\varepsilon} \le 1\ s^{-1} \\ \beta\left(\dot{\varepsilon}/\dot{\varepsilon}_s\right)^{3/4}, & \dot{\varepsilon} > 1\ s^{-1} \end{cases} \qquad (2.4)$$

Two studies reported modulus of elasticity for UHPC based on direct tension tests with up to 3% steel fiber reinforcements. The authors reported that the modulus of elasticity of UHPC is not rate sensitive between 10^{-4} and 10^{-1} s^{-1}. Seven studies listed discussed the effect of strain rate capacity corresponding to the ultimate tensile strength

and these studies are in good agreement with one another except one. The authors proposed the improved model as in Eq. (2.5) (Thomas and Sorensen, 2017).

$$\mathrm{DIF}_{\varepsilon t} = \begin{cases} \left(\dot{\varepsilon}/\dot{\varepsilon}_s\right)^{1/121}, & \dot{\varepsilon} \le 20\ s^{-1} \\ \beta\left(\dot{\varepsilon}/\dot{\varepsilon}_s\right)^{1.5}, & \dot{\varepsilon} > 20\ s^{-1} \end{cases} \qquad (2.5)$$

Based on the eight studies that reported energy absorption during tensile loading for UHPC the author proposes an improved model in Eq. (2.6) (Thomas and Sorensen, 2017).

$$\mathrm{DIF}_{g} = \begin{cases} \left(\dot{\varepsilon}/\dot{\varepsilon}_s\right)^{1/121}, & \dot{\varepsilon} \le 25\ s^{-1} \\ \beta\left(\dot{\varepsilon}/\dot{\varepsilon}_s\right)^{1.8}, & \dot{\varepsilon} > 25\ s^{-1} \end{cases} \qquad (2.6)$$

Othman et al. (2019) reported the loading rate dependency of compressive strength, elastic modulus, and flexural strength of UHP-FRC. They tested five UHP-FRC series with three different matrix strength ranging from 16-21.8 ksi (110-150 MPa) and three different fiber volume content. Six different strain rate ranging from quasi-static to impact level was used in their investigation. They reported improved compressive strength, elastic modulus, flexural strength, and post-cracking response with increase matrix strength for same fiber content by volume. Fiber content volume was observed to significantly increase post-ductility in flexural test. Compressive strength and elastic modulus was reported to be insignificantly affected by fiber volume. Authors reported increase mechanical performance of the material as increased strain rate. The DIF was found to be higher for matrices with lower compressive strength, for both compressive strength and modulus of elasticity. However, DIF was reported to be different for

compressive strength and elastic modulus. Fiber volume content showed no effect of dynamic enhancement of the above mentioned properties. Compared to elastic modulus and compressive strength, the flexural strength was reported to be more sensitive to strain rate. The paper reported that the dynamic enhancement to be inversely proportional to fiber content (Othman et al., 2019).

2.4 Structural Performance

While discussing the structural behavior of reinforced UHPC beams under flexure, Yoo and Yoon (2015) reported that the inclusion of steel fibers caused decreased first cracking load and deflection. Also, the first cracking load slightly decreased with an increase in reinforcement ratio. It was reported that the flexural stiffness before the occurrence of first cracking was insignificantly influenced by steel fibers. Both smooth and twisted steel fibers substantially improved the post cracking stiffness and peak load. Improved flexural capacity can be obtained by the inclusion of steel fibers due to the bridging capacity of fibers. The reinforcement ratio increased the load carrying capacity. Reinforcement ratio had no noticeable effect in the load carrying capacity and post-cracking stiffness. The authors reported that the ductility index decreased with an increase of reinforcement ratio for the beam specimens without fibers. The magnitude of decrease in ductility by including steel fibers increased with the application of lower reinforcement ratio. Longer fibers resulted in higher ductility. Vertical flexure cracks formed perpendicular to the maximum principle stress direction after the cracking moment. Cracks in the beam without fibers propagated more deeply into the compression zone than the cracks in the beams with steel fibers at a low applied load of 40 kN.

However, the beams with steel fibers exhibited flexural cracks with very short depths due to bridging effect. When the applied load exceeded approximately 60 kN, the number of cracks within the beam without fibers slightly increased and the crack widths continuously increased. For the beams with fibers, continuous increase in the number of crack was observed until near the peak load. The increase of crack width was insignificant. Most of the cracks gradually propagated to the compression zone without any visual widening. Failure of the beams without fiber caused by concrete crushing in the compression zone. The beams with steel fibers showed fiber pullout at one or two specific cracks near peak load and then the width of this specific cracks increased significantly compared to other cracks. The average crack spacing in the beams with steel fibers rapidly decreased with an increase in the load at the low load stage and became stable after reaching approximately 50% of the peak load. The beams without fiber showed almost identical crack spacing with an increase in the load. The tests showed that the length and type of fibers for the structural beams with steel rebar influenced the cracking response and crack distribution insignificantly. The number of cracks increased noticeably with an increase in the fiber length (Yoo and Yoon, 2015).

2.5 Impact and Blast Load on UHPC

In 2015, a series of tests were run on reinforced UHPC and normal strength concrete slabs to study their response under explosive loading. Five slabs were tested with varying reinforcement ratios. A normal strength concrete slab was tested as a control sample. The authors modeled the experimental results of UHPC under blast loads using LS-DYNA (Li et al., 2015).

The authors performed laboratory uniaxial compression tests on cylindrical UHPC and NSC samples and obtained stress-strain relationship. Under the blast loads, various damage modes such as flexural damage, combined shear and flexural damage were observed. Ductal® type of UHPC was used in all the constructions. The dimension (7.9/39.4/3.9 inch or 200/1000/100 mm) were identical for all the slabs. Steel fibers were used by 2% volume fraction. 0.8% reinforcement ratio were used in all UHPC and NSC slabs except one. Three types of steel bar were used. The explosive charges were reported as TNT equivalent weight ranging from 2.2 lbs. to 30.86 lbs. (1.0 to 14.0 kg). The scaled distance ranged from 1.03 to 7.7 ft./$lbs^{1/3}$ (0.41 to 3.05 m/$kg^{1/3}$). The UHPC slabs were referenced with unique identifiers beginning with 'D' and followed by a number from 1 to 4. The UHPC-D3 slab was designed for two explosives and designated with A and B. The permanent deflection of the slabs increased as the scaled distance decreases. The member response shifted from elastic to plastic range and then to failure. The authors noted by comparing between UHPC-D1 and UHPC-D3B that under the same blast scenario, the reinforcement plays significant role in resisting overall damage. UHPC-D3B with mild steel reinforcement of 43.5ksi (300 MPa) yielding strength, collapsed completely. UHPC-D1 with a reinforcement of 87 ksi (600 MPa) yield strength experienced plastic damage but not complete failure. The authors reached the same conclusion for UHPC-D2 (253.8 ksi yield strength) and UHPC-D4 (43.5 ksi). The former one had almost no damage while the late one experienced significant midspan deflection and plastic flexural damage. For NSC-1 slab, large fragmentation at midspan was observed. Concrete spall and fragment were not observed in UHPC-3B and UHPC-4.

These specimens were subjected to even severe blast load. This result is attributed to the bridging effect of steel fibers. The UHPC-D2 had high steel reinforcement ratio and performed best (Li et al., 2015).

Eight node hexahedron solid elements were used for numerical modelling of UHPC in LS-DYNA. Flanagan-Belytschko based hourglass control option was used with hourglass coefficient 0.1. Hughes-Liu beam element with cross section integration was used to model steel reinforcement. MAT_Elastic_Plastic_Hydrodynamic material model was adopted for modelling UHPC. Young's modulus obtained from cylinder test was used to define the elastic deformation phase. To capture the initiation and propagation of concrete material damage, Numerical Erosion Algorithm was adopted. Steel reinforcement is simulated by MAT_Piecewise_Linear_Plasticity. Due to lack of test data, strength enhancement in the UHPC material was not included. The authors used the built-in Load_Blast function in LS-DYNA to model blast load. The finite element model reproduced the structural damage under blast load with reasonable accuracy. The authors suggested that the model could be further revised by adding the effect of strain rate on UHPC material (Li et al., 2015).

In 2012 Yi et al. investigated the material properties and blast resistant capacities of ultra-high strength concrete (UHSC) and reactive powder concrete (RPC). On reinforced UHSC and RPC panels, ANFO blast tests were performed. For the experimental program, normal strength concrete (NSC), UHSC and RPC panels were tested. Special short steel fibers at 2% volume were added in RPC specimens. To investigate blast-resistant capacity of reinforced UHSC and RPC panels, ANFO blast

loading was adopted. Based on preliminary tests, 35 lbs. (15.88 kg) of ANFO and a standoff distance of 4.6 ft (1.4 m) were selected for main tests. The panel dimensions are 39.4×39.4×5.9 inch (1000×1000×150 mm) with two layers of D10 mesh reinforcement at a 3.22 inch (82 mm) spacing in both directions were placed in the NSC and UHSC panels. Short steel fibers at a 2%-vol. was used for RPC specimens. Blast pressures, deflections, strains and wave impact accelerations of all the specimens were measured under blast loading. In NSC specimens, well dispersed turtle back types of crack patterns were observed. From the center to four corners macro crack similar to a cone prism type of plastic yield line were observed. This indicates a two dimensional membrane plastic failure mode. Diagonal shear cracks formed on the side surfaces of the specimens suggested that the panels were susceptible to shear failure. The authors mention no damage or crack on the top surface of UHSC and RPC panels, indicating greater resistance than NSC specimens. The RPC specimens were bisected in the middle by one-directional multiple chopped macro cracks. The authors concluded that UHSC and RPC failed in brittle manner even under flexural mode based on their failure due to micro cracks. Overall, the UHSC and RPC were more resistant than NSC panels, whereas RPC had the best blast-resistant capacity. In addition, RPC specimens were prone to have smaller deflections and cracks compared to other specimens reinforced only with ordinary bars. Strain in steel could not be measured for RPC specimens as they lack reinforcing bars. Maximum strain at bottom reinforcement is measured. The test results indicated smaller displacement in UHSC specimens than NSC one. Strain at the center of RPC specimens was found to be less than that of NSC and UHSC specimens due to the

presence of short steel fibers in RPC one. Reinforcement in UHSC and RPC caused larger strains but did not control cracks. The wave acceleration measurement data showed that the RPC specimen was markedly different and was characterized by large oscillations and magnitude. Possible reasons can be either the reinforcing bars in NSC and UHSC specimens controlled the structural acceleration behavior or that RPC with steel fibers is more flexible than UHSC and absorbs more energy. Finally, the Fast Fourier Transform spectrum analysis data showed identical resonant frequencies for all types of specimens, though the magnitude of amplitude varied. RPC specimens vibrated with acceleration over a short duration as the short steel fibers made it very flexible (Yi et al., 2012).

Farnam et al. (2010) investigated High Performance Fiber Reinforced Cement (HPFRC) panels by drop projectile up to an impact at which failure occurs. Mechanical properties obtained from experimental investigation were used to define parameters for numerical model in LS-DYNA. A drop-weight impact testing apparatus was used for impact test. A cylindrical projectile with 2-inch diameter, 21.65-inch height and 18.74 lbs. weight (50 mm diameter, 550 mm height and 8.5 kg weight) was used. The projectile was dropped from 3.28 ft. (1 m) height. During the test, plain concrete specimen failed in the first strike with a circular shear punching and fragmented into seven pieces. Some cracks were generated near the corners of the panel in truncated circular shapes due to boundary condition. For HPFRC specimens, radial flexural micro cracks formed in the first strike and propagated in next strikes. Punching failure was observed and enlarged with the effect of circular micro cracks in the two final strikes. The governing mode of

failure was shear punching failure. The punching failure occurred in a truncated cone shape. The upper diameter of the cone was smaller than the lower one. For the fourth HPFRC specimen, the failure was nor in a circular symmetric shape. All HPFRC, except for the first specimen, resisted up to five strikes. The discrepancy for the first specimen was attributed to improper fixture. The second specimen reached the threshold of failure in the fifth strike and further resisted well into the sixth strike (Farnam et al., 2010).

In LS-DYNA, the FE models were generated with the pre-processor FEMB ver.28 and analyzed with the solver LS-DYNA ver.971. Post processing of the results were performed with LS-PREPODT ver.2.1. Hexahedron elements were used to mesh panels and the projectile. Tetrahedron elements were used to model rigid constraints. CONTACT_AUTOMATIC_SURFACE_TO_SURFACE option was adopted to define the contacts between the projectile and the panel as well as between the panels and the constraints. To handle contact/impact phenomena, penalty method was used with a penalty factor 0.9. Restart analysis was performed with a new impact after completion of each strike to model periodic impact loading. The outputs at the end of each impact were assumed as the input state for the next impact. SOIL_CONCRETE model was adopted to simulate FRC behavior. Material properties obtained from mechanical tests were used in FE-model. Based on previous studies, few of the required data were assumed for numerical model. MAT_ADD_EROSION option was used with an ultimate shear strain of 0.012 for HPFRC. For modeling constraints of impact test setup and the projectile, a linear elastic model was used. Five strikes were simulated with five restart analysis (Farnam et al., 2010).

In the simulation, plain concrete failed in the first strike with seven divided parts, similar to the experiment. Both flexural and shear punching cracks were observed in radial and circular cracks, respectively. Some truncated circular shaped cracks were observed near the corners of the model. Although they were much less than the experimental corner cracks. The panels in FE-model endured five strikes, which was equal to that for third and fourth specimens. Average midpoint deflection on the bottom surface and trends of crack growth from simulation and experiments showed good agreement. The authors reported that the numerical results for the first, second, and fourth strikes were slightly overestimated and for the third strike, it is slightly underestimated. Flexural cracks and punching failure patterns were similar to the test results (Farnam et al., 2010).

2.6 Summary

This chapter provide the background study of the development, mechanical properties, structural performance, and performance under blast loads. The significant themes of can be summarized as:

1. UHPC is a promising material which is gaining significant attention due to its higher compressive strength as well as other mechanical properties. Over the last three decades, researchers have extensively studied its properties and possible use in structural systems. Several commercially available variants of this material are available in the market.

2. Studies shows that UHPC is superior compared to conventional concrete in terms of compressive, tensile and flexural behavior. Ductility can be improved by adding steel fibers. Size and geometry of the specimens, fiber type, length, placement methods, and fiber content significantly affect the performance of UHPC and UHPFRC.
3. The strain rate sensitivity of the tensile properties of UHPC is similar to that of conventional concrete at quasi-static and intermediate strain rates. However, UHPC is much more strain rate-sensitive than conventional concretes at high strain rates. The strain rate sensitivity of UHPC is independent of fiber volume, fiber geometry, fiber factor, or compressive strength.
4. Addition of steel fibers improves the load carrying capacity, post-cracking stiffness, and cracking response, while decreases ductility. Length and type of steel fibers (twisted or smooth) affect the structural performance of UHPC considerably.
5. Under high loading rates, UHPC performs better compared to normal strength concrete. Incorporation of fibers can increase the tensile strength, energy absorption capacity, toughness, ductility and other properties of UHPC. Thus, the promise of this material is very high for strategic structures those need protection against high impact and blast loads.

CHAPTER 3

METHODOLOGY

3.1 Introduction

In order to study the contribution of each mixture component to the mechanical behavior of high strength concretes a non-proprietary mix is needed. For this experimental program, a UHPC mix design from previous researchers is selected as a baseline control mix (Thomas et al., 2017). Based on that mix design, different batches of HSCM with parametric variations are prepared and tested. Multiple standards and methods from ASTM and other researchers are considered for the preparation and test of specimens. Normal Portland cement, silica fume, local sand and silica sand, and HRWR superplasticizer for workability are used in each batch. The mix parameters varied parametrically throughout different phases of experiments are water to binder ratio, silica fume percentage, and sand fraction. Compressive strength test and Charpy impact test are employed to investigate the properties of the material and contribution of different components of it.

3.2 Outline of Experimental Program

The experimental program described in this thesis is conducted in two phases- HSCM with constant paste volume with parametric change and HSCM with different sand fractions. Paste volume of concrete is the total volume of cementitious material and the volume of water. Cement is the most expensive component of concrete, while, usually, aggregate is the cheapest. Cementitious materials and water create the paste

which coat the aggregates, fill voids, and binds them. But excess cement paste also causes problems, such as, shrinkage cracking, excess heat, high dosage of expensive admixture as well as higher carbon footprint. Thus, it is the interest of many researches to optimize concrete by reducing cement paste and maximizing aggregate volume. For conventional concrete, total volume consists of 15-30% of paste (water and binder) and 65-80% of aggregates. In UHPC, larger surface area resulting from smaller aggregates, is required to be enveloped by cement paste. This results in higher paste volume. Existing literature shows paste volume in range of 35-70% (Ma et al., 2004; Reda et al., 1999; Yalçınkaya and Yazıcı, 2017). Similar to UHPC, the HSCM used in this study is devoid of coarse aggregate, and therefore, has high paste volume. Although, this research project does not aim to optimize the mix design, keeping an eye to future research, the paste volume of HSCM is kept constant. For the first phase of this research, a constant paste volume of 70% is chosen. The silica fume, water-binder ratio, and sand fractions are varied in such a way to keep the paste volume at constant. After completing the initial phase, it was evident the desired strength of 18 ksi is not achieved with local low quality sands. Therefore, for next phase, nationally available high quality quartz and silica sands are procured and effect of sand fraction and gradation are studied.

3.3 Materials

Cement, silica fume, sand, and superplasticizer used in this research are shown in Figure 3.1. Cement used for the research program is Ordinary Portland Cement (OPC) conforming ASTM C150-16 Standard Specification for Portland Cement (ASTM, 2016) for type II-V cement. Norchem un-densified silica fume is used. The silica fume

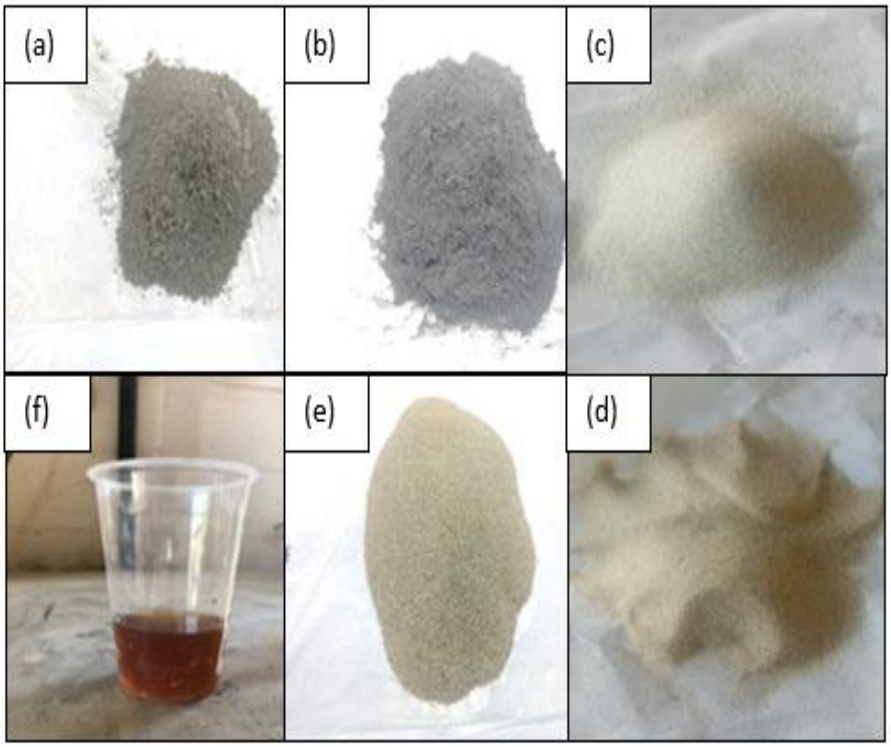

Figure 3.1: (a) Cement, (b) Silica Fume, (c) Quartz Sand, (d) Silica Sand, (e) Local Sand, and (f) Superplasticizer

conforms to ASTM C 1240-15 Standard Specification for Silica Fume Used in Cementitious Mixtures (ASTM, 2015). To achieve necessary workability, MasterGlenium 3030, a full-range water-reducing admixture meeting ASTM C494 / C494M - 17, Standard Specification for Chemical Admixtures for Concrete (ASTM, 2017), is used. The sand used for the first stage of the experiment is collected from a local supplier. The gradation of the sand is such that the maximum particle size for different batches are 0.0117 inch (0.297 mm), 0.0165 inch (0.420 mm), and 0.0234 inch (0.595 mm).

For the second phase of the research, nationally commercially available quartz and silica sands are used in the control mix, provided by Granusil and US silica. The

gradations of the sands are determined using Malvern Instruments Mastersizer 2000 laser particle size analyzer. This device can analyze grain sizes ranging from 0.1 micron to 1000 microns (clay to coarse sand). The gradation curves, obtained by analyzing the data from laser particle size analyzer, are provided in Appendix A. The mixes used a wide range of water-cement ratios to find one with maximum compressive strength, which can be later improved to be qualified as a UHPC mix.

3.4 Mix Design

The first phase of the experimental program area is performed using locally available material. Based on a previous research, the control mix of the experimental program is chosen (Thomas et al., 2017). That research, in turn, was based on another paper on developing UHPC with locally available material (Allena and Newtson, 2011). Using the procedure and mix proportion outlined by Thomas et al., the mix proportions are varied to prepare 15 batches of mixes with constant paste volume of 70%. The mix proportions of the all the batches are given in Table 3.1. The first batch (P1-1) is the control mix. For rest of the batches, silica fume replacement ratio, water to binder ratio, maximum particle size, and sand fractions are varied parametrically. These15 batches are used to cast 2 inch cubic specimens for compression tests and 2×1×0.5 inch notched Charpy impact specimens. The compression tests are performed at 4 strain rates ranging from quasi-static (10^{-4} per second) to blast loading (10^{-1} per second) (Hentz et al. 2004). The Charpy impact test is conducted using two latch position with impact velocities of 10.83 ft/sec and 16.73 ft/sec.

Table 3.1:Parametric Mix Proportion for Phase 1 (per one cubic yard)

Batch Id	Cement (lb./yd^3)	Silica Fume (lb./yd^3)	Water (lb./yd^3)	Sand (lb./yd^3)	Superplasticizer (gal/yd^3)	Sand Passing Sieve
P1-1	1738.8	434.7	434.7	1340.0	6.51	100% Passing #50
P1-2	1877.1	469.3	375.4	1340.0	7.03	100% Passing #50
P1-3	1805.3	451.3	406.2	1340.0	6.76	100% Passing #50
P1-4	1677.0	419.2	461.2	1340.0	6.28	100% Passing #50
P1-5	1619.5	404.9	485.8	1340.0	6.06	100% Passing #50
P1-6	2003.0	222.6	445.1	1340.0	6.67	100% Passing #50
P1-7	1869.3	329.9	439.8	1340.0	6.59	100% Passing #50
P1-8	1611.3	537.1	429.7	1340.0	6.44	100% Passing #50
P1-9	1486.7	637.1	424.8	1340.0	6.36	100% Passing #50
P1-10	1738.8	434.7	434.7	1340.0	6.51	50% Passing #30, 50% Passing #50
P1-11	1738.8	434.7	434.7	1340.0	6.51	50% Passing #40, 50% Passing #50
P1-12	1863.0	465.7	465.7	1116.7	6.98	100% Passing #50
P1-13	1738.8	434.7	434.7	1340.0	6.51	100% Passing #50
P1-14	1987.2	496.8	496.8	893.3	7.44	100% Passing #50
P1-15	2235.6	558.9	558.9	446.7	8.37	100% Passing #50

Color Code			
	Control Mix	Mix with different water-binder ratio	Mix with different silica fume fraction
	Mix with different maximum sand particle size		Mix with different sand fraction

After completing the first stage of the experimental program, it became evident that the target strength of 18,000 psi was not achievable with either the current materials, mix proportions, or procedure, as shown in Chapter 4. The research then shifted focus on isolating the contribution of different components of the mix. With that goal, 5 industrial grade quartz sands and 3 silica sands are procured from two sources and incorporated into the mix design. The sands are used to prepare 8 batches of mixes with the same mix proportions as the control mix, and tested for compressive strength according to C39/C39M-14: Standard Test Method for Compressive Strength of Cylindrical Concrete Specimens (ASTM, 2016). These mixes are to find the strength variation of UHPC using manufacturer supplied sands with different gradation available in the market. Then 5 batches for quartz sand and 5 batches of silica sand with different sand fractions are considered for compressive strength at different strain rate and Charpy test. To make these batches, the sand is sieved down to No. 50 sieve (maximum particle size 0.0117 inch). The mix proportions are provided in Table 3.2.

Table 3.2:Mix Proportions for Different Sand Fraction (Phase 2)

Batch Id	Cement (lb./yd^3)	Silica Fume (lb./yd^3)	Water (lb./yd^3)	Sand (lb./yd^3)	Superplasticizer (gal/yd^3)	Sand Passing Sieve
P2-1	1738.8	1738.8	1738.8	1738.8	1738.8	100% Passing #50
P2-2	434.7	434.7	434.7	434.7	434.7	100% Passing #50
P2-3	434.7	434.7	434.7	434.7	434.7	100% Passing #50
P2-4	1340.0	1340.0	1340.0	1340.0	1340.0	100% Passing #50

3.5 Mixing Procedure

During the mixing procedure, the cement, sand, and silica fume are mixed together to obtain a uniform mix with a commercial food mixing machine. Superplasticizer is mixed with water before adding the cement, sand and silica fume mixture. Water is added to the mix while the machine is running. The mixing machine, manufactured by Avantco Equipment, operates in three speeds: 156, 258, and 508 rpm. The model is MX 10.

3.5.1 Casting and Curing Specimens

In this research project, casting and curing procedure for UHPC mix is followed. Mixing machine and mold are shown in Figure 3.2. Casting and curing procedures for UHPC mix differ from those of conventional concrete. Also, Charpy impact test is not standardize for cementitious materials. Therefore, adjustments and modification for preparation of Charpy specimens are required.

ASTM C 1856-17, Fabricating and Testing Specimens of Ultra-High Performance Concrete requires 75 mm by 150 mm (3 in. by 6 in.) cylindrical specimens for compressive strength test of UHPC. It also prohibits using capping compound and un-bonded neoprene pads (ASTM, 2017). Instead, it requires that end of the cylinders shall be ground plane to within 0.050 mm. ASTM C192 / C192M - 18, Standard Practice for Making and Curing Concrete Test Specimens in the Laboratory specifies either 100 mm by 200 mm (4 in. by 8 in.) or 150 mm by 300 mm (6 in. by 12 in.) cylinders (ASTM, 2018). This standard also refers to ASTM C617 / C617M - 15, Standard Practice for

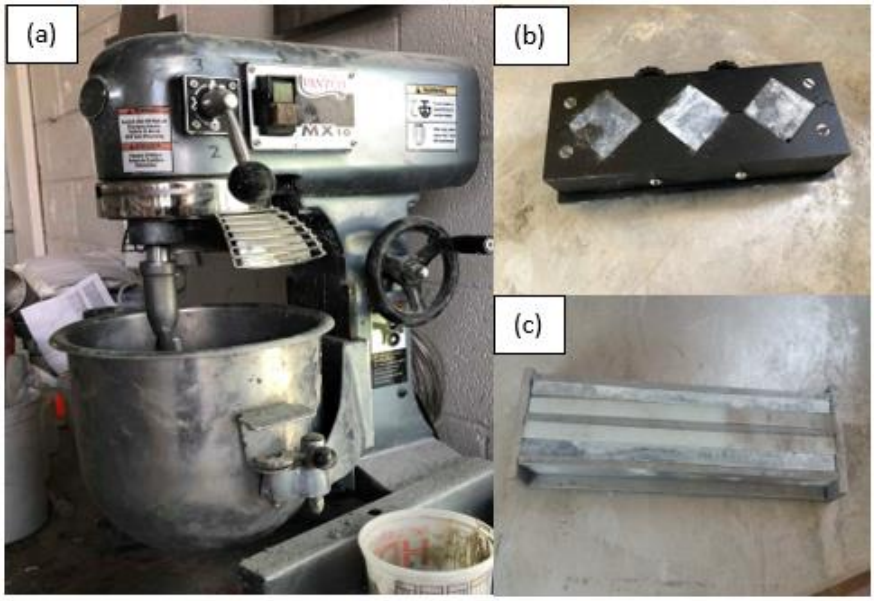

Figure 3.2: (a) Mixing Machine, (b) Compression Specimen Mold, and (c) Charpy Specimen Mold

Capping Cylindrical Concrete Specimens which specifies high-strength gypsum paste or Sulphur based capping material (ASTM, 2015). But it should be noted that the strength of the capping material is not compatible with the expected strength of HSCM and UHPC. For this reason, the necessity of a different casting and testing method was felt at the time of designing the program.

As this research program was designed before the publication of ASTM C 1856-17, this standard is not followed. The test specimens are 2 inch (50 mm) cubic samples prepared according to ASTM C617 / C617M - 15, Standard Practice for Capping Cylindrical Concrete Specimens (ASTM, 2015). The mixing and curing procedure for HSCM cubes is as follows:

1. Weigh the cement, sand with appropriate gradation, and silica fume. Mix the dry ingredients thoroughly for a few minutes in the bowl of a food mixing machine.

2. Weigh water and superplasticizer and mix them together.
3. Add all of the water and superplasticizer with the dry ingredients and mix them with a spatula. Start the mixing machine at a low speed for 5-7 minutes.
4. Mix for approximately another 10 minutes at moderate speed.
5. Run the mixing machine for another 10 minutes. Look for a consistent texture and then stop.
6. Run the mixing machine for another 5 minutes. Look for a consistent texture and then stop.
7. The molds, for both compression and Charpy test specimens, are filled in two lifts.
8. Fill half of the molds for the Charpy test specimen and 2 inch (50 mm) cubes. Vibrate the half-filled molds for 1 minute. Before filling the molds, WD-40 is applied to ensure simple removal of the specimens.
9. Fill rest of the molds, and vibrate again for 1 minute.
10. Level the top surface of each mold with a wet trowel. Cover the molds with a plastic paper. Place a petri dish filled with water under the cover.
11. After 24 hours, the specimens are removed from the molds and placed in a lime water bath at 50℃ temperature for 25 days.
12. After 25 days, place the specimens in an oven at 250℃ for 2 days.
13. Test after the specimens cool to room temperature.

3.6 Test Procedure

This section describes the testing procedure used for both the compression and Charpy testing.

3.6.1 Compression Test

The Universal Testing Machine used for compression test as well as test set up and a specimen at failure is shown in Figure 3.3. Number of specimens tested at various strain rates for Phase 1 is presented in Table 3.3. Compression tests on HSCM cubes are done at 4 strain rates: $10^{-4}\ s^{-1}$, $10^{-3}\ s^{-1}$, $10^{-2}\ s^{-1}$, and $10^{-1}\ s^{-1}$. Additionally, these batches are tested according to ASTM C 39 standard test method. The specimen width, length, and height are measured during the test to find the cross sectional area. Then the specimens are

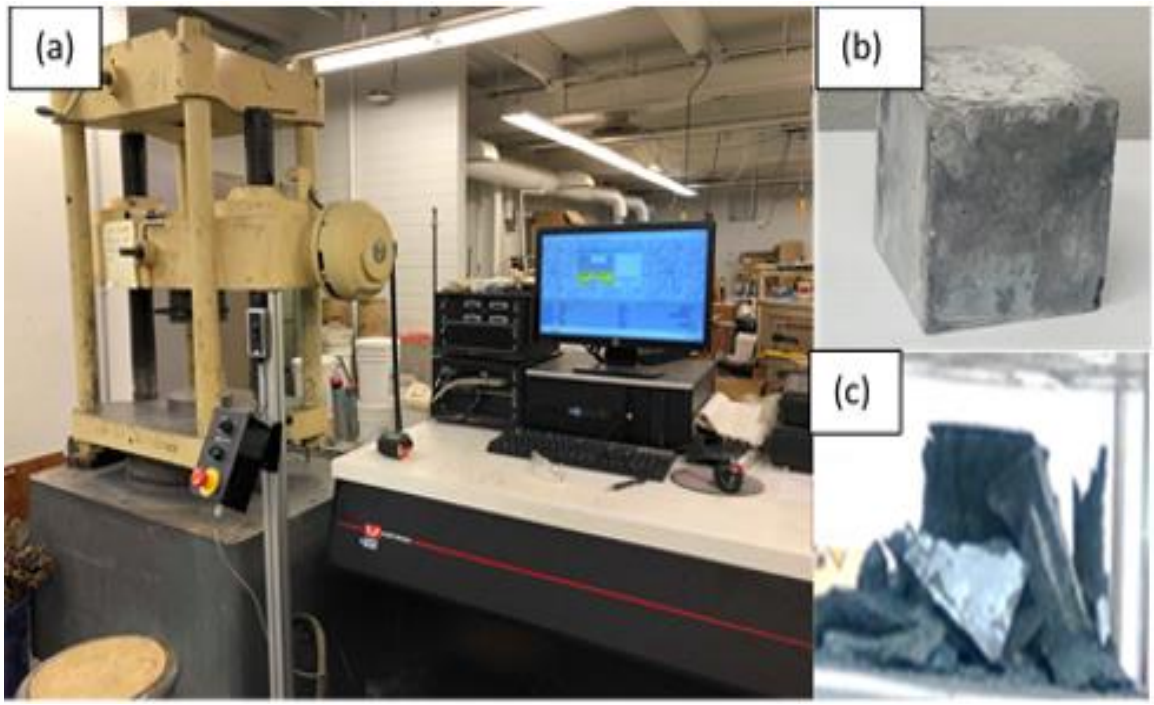

Figure 3.3:(a) Universal Testing Machine, (b) Compression Specimen, and (c) Specimen at Failure

placed on the loading platen of the compression machine after wiping both top and bottom surface with WD-40. It is made sure that the troweled surface of the cube, which is the least smooth face, is placed on a non-loading side so that the load is applied on the smoother surface.

Table 3.3:Number of Specimens Tested at Various Strain Rates for Phase 1

Batch	Strain Rate (s^{-1})			
	10^{-4}	10^{-3}	10^{-2}	10^{-1}
P1-1	2	3	2	2
P1-2	3	3	3	3
P1-3	3	3	3	4
P1-4	3	3	3	3
P1-5	3	3	3	2
P1-6	3	3	3	3
P1-7	3	3	3	3
P1-8	3	3	3	3
P1-9	3	3	3	3
P1-10	3	3	3	3
P1-11	3	3	3	3
P1-12	3	3	3	3
P1-13	3	3	3	3
P1-14	3	3	3	3
P1-15	3	3	3	3

The Universal Testing Machine (UTM) is manufactured by Tinius Olsen with a capacity of 300,000 lbs. The software interface is provided by Instron. Through the

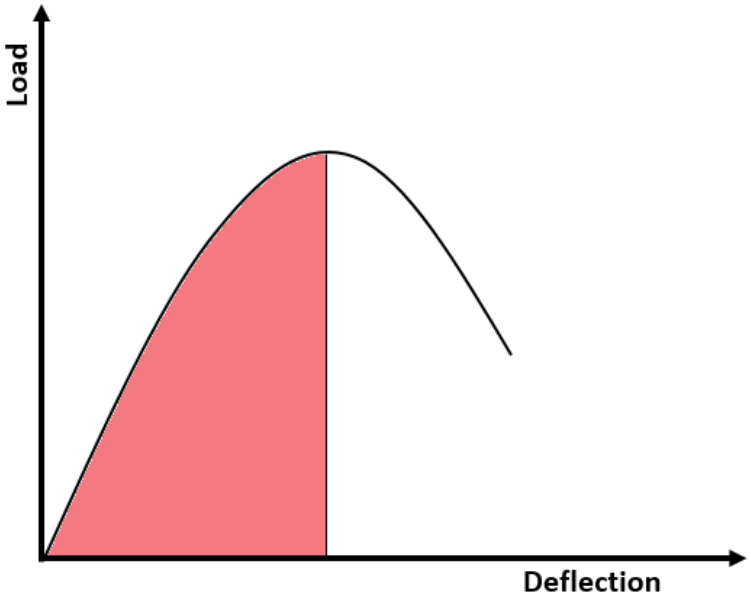

Figure 3.4: Calculation of compressive toughness

software interface, the machine can be operated in a strain controlled setting. The compressive load is applied until the specimen can resist 80% of the maximum load applied. The strain rate is maintained with a computer, which displays the maximum stress and peak load. Results from the software interface come in form of a comma separated value (csv) file, containing the load, position, stress, and strain data. Strain is calculated by the software from the position of the loading platen.

To calculate compressive toughness of a specimen, load-deflection data is collected from the UTM. Then the area under the load-deflection curve up to peak load (Figure 3.4) is calculated by using numerical integration. This are is then normalized with respect to the volume of each specimen to calculate the compressive toughness of the material.

The number of Specimen tested for Phase 2 are given in Table 3.4.

Table 3.4: Number of Specimens Tested at Various Strain Rates for Phase 2

Batch	Strain Rate (s^{-1})			
	10^{-4}	10^{-3}	10^{-2}	10^{-1}
P2-1	3	3	3	3
P2-2	3	3	3	3
P2-3	3	3	3	3
P2-4	3	3	2	3

3.6.2 Charpy Impact Test

Charpy Impact Test provides a model of impact load on concrete specimen. ASTM E23 - 18 Standard Test Methods for Notched Bar Impact Testing of Metallic Materials is modified to test cementitious specimens (ASTM, 2018). Thomas and Sorensen suggest minimum specimen dimension to be no smaller than five times the characteristic size of the largest constituents. For notched specimen, then suggest saw-cut notch in hardened concrete (Sorensen and Thomas, 2018). Both of these recommendations are followed in this research.

The Charpy Impact Testing machine (Model DI-300) used is manufactured by Instron. The machine releases a hammer, weighing 13.33 lbs., can be set to low or high latch position. By setting the hammer at a particular position, a specified amount of potential energy is stored in the impacting machine. These two positions store a potential energy of 25 ft-lbf. and 60 ft-lbf, respectively. When the hammer is released, the potential energy is converted to kinetic energy, which breaks the specimen. The energy absorbed by the specimen is calculated from the difference in the of height of the hammer before and after fracture, corrected for friction and air resistance.

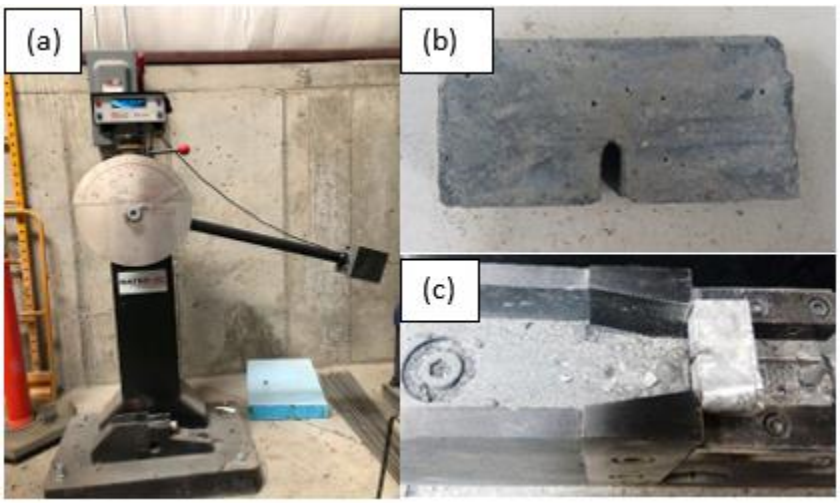

Figure 3.5: (a) Charpy Impact Testing Machine, (b) Charpy Specimen, (c) Charpy Test Setup

The specimens are cut in to 2-inch length. A notch of approximately 0.3 inch is cut at mid length to provide a weak plane to break the specimen at a desired location. The specimen is placed in the machine such that the notch is facing outward. The height and width at the notch of the specimens are recorded before the test. The apparatus is calibrated before testing each batch to account for friction and air resistance. The hammer, weighing 13.33 pounds, of the machine is dropped from two known heights.

As the hammer is released, the potential energy of the hammer is converted to kinetic energy. At the point of impact, part of the energy is absorbed by the specimen as it breaks. Then the impact energy absorbed can be calculated from the lost potential energy once adjusted for the loss due to friction and air resistance. This is automatically performed by the device and shown directly in a digital display. From the test, the impact energy absorption is calculated. The test setup is shown in Figure 3.4.

The energy absorbed by specimens are normalized with respect to cross-sectional area of failure plane. The equation to calculate the normalized energy absorbed (toughness) is given in Equation 4.1:

$$E_{impact} = \frac{E_o}{t * (w - d_{notch})} \quad (3.1)$$

Where,

$E_{impact} = Normalized\ Impact\ Energy\ absorbed\ \left(\frac{inch - lb}{in^2}\right)$

$E_o = Impact\ Energy\ Absorbed\ (inch - lb)$

$t, w = Thickness\ and\ width\ of\ the\ Specimen\ (inch)$

$d_{notch} = Notch\ Depth\ (inch)$

Number of Charpy impact tested specimen tested for both phased are given in Table 3.5 and 3.6.

Table 3.5: Number of Charpy Specimens Tested for Phase 1

Batch	Impact Velocity	
	10.83 (ft/sec)	16.73 (ft/sec)
P1-1	10	9
P1-2	7	7
P1-3	9	9
P1-4	9	9
P1-5	10	10
P1-6	8	9
P1-7	9	10
P1-8	7	8

Batch	Impact Velocity	
	10.83 (ft/sec)	16.73 (ft/sec)
P1-9	7	8
P1-10	8	9
P1-11	10	9
P1-12	9	10
P1-13	8	8
P1-14	8	9
P1-15	9	10

Table 3.6: Number of Charpy Specimens Tested for Phase 1

Batch	Impact Velocity			
	Quartz Sand		Silica Sand	
	10.83 (ft/sec)	16.73 (ft/sec)	10.83 (ft/sec)	16.73 (ft/sec)
P2-1	9	8	7	6
P2-2	7	7	6	10
P2-3	8	7	8	9
P2-4	7	8	9	7

CHAPTER 4

LABORATORY TEST RESULTS

4.1 Introduction

This chapter presents the results of the specimens prepared according to the methodology outlined in Chapter 3. Specimens are tested in compression at different strain rates and also tested for their dynamic shear energy absorption capacity using the Charpy impact testing method.

This chapter is divided into three main sections, which are further divided into subsections. The main sections are: HSCM mix with constant paste volume, HSCM mix with manufacturer supplied sand, and HSCM mix with different sand fraction. The subsections, in general, present compressive strength, and dynamic shear energy absorption results obtained from laboratory testing. Average compressive strength and impact toughness is presented in plots, along with standard deviations.

4.2 HSCM with Constant Paste Volume

Initially 15 batches of HSCM mixes with 70% paste volume are cast to test compressive and impact energy absorption tests using a locally available sand. The mix proportions of these batches are varied in order to isolate the contribution of each component. The Charpy impact test is also performed and, finally, a correlation between compressive strength and energy absorption is sought.

4.2.1 Compressive Strength

To investigate the effect of water-binder ratio, five batches of HSCM specimens with constant paste volume are tested and presented. As the HSCM mix has very low water-binder ratio, during the tests, it is varied between 0.16 and 0.24.

Figure 4.1 illustrates the trend observed from these tests. As water-binder ratio is increased, generally, the strength is decreased. This conforms to the general behavior of cementitious composites. Apart from strain rate of 10^{-4}/s, maximum compressive strength is achieved at w/binder ratio of 0.2, indicating the optimum ratio. The maximum compressive strength is achieved at the maximum w/binder ratio of 0.24 at the highest strain rate. This result seems to be an outlier. Overall, the results show high sensitivity of compressive strength to water-binder ratio.

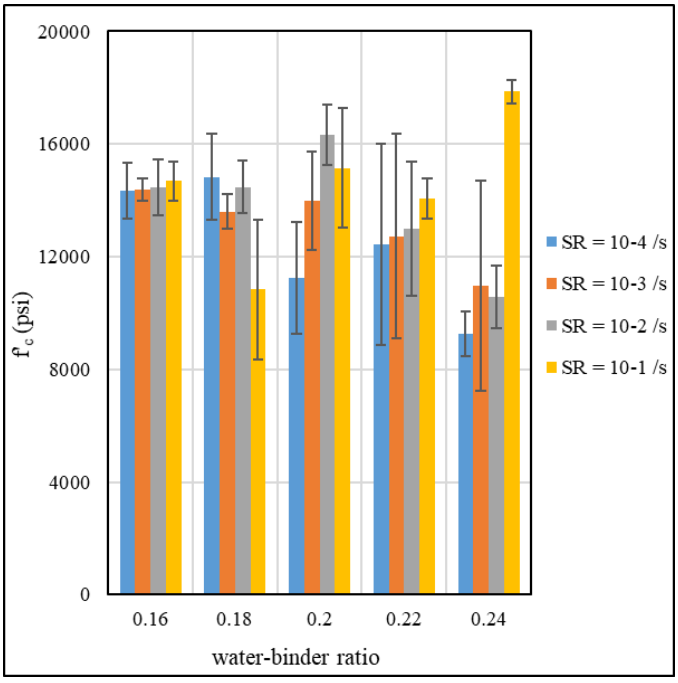

Figure 4.1:Variation of average compressive strength with water-binder ratio for HSCM with constant paste volume

Variation of compressive strength at different strain rate for different silica fume replacement ratio is illustrated in Figure 4.2. Researches have shown multiple functions of silica fume in high strength concrete, such as, UHPC. It fills the micro voids, initiates secondary hydration at higher curing temperatures, and contribute to create the dense matrix. As detailed in Chapter 3, five silica fume to binder ratios, ranging from 0.1 to 0.3, are used to investigate the contribution of this parameter for a constant paste volume mix. In this research, by changing the silica fume replacement, no general trend on the compressive strength is observed, therefore no conclusion is reached. The scatter of data and findings from previous researches suggest more testing is required.

To investigate the contribution of sand fraction, five batches of HSCM are tested, as stated in the previous chapter, and test results are presented in Figure 4.3. Local sand is

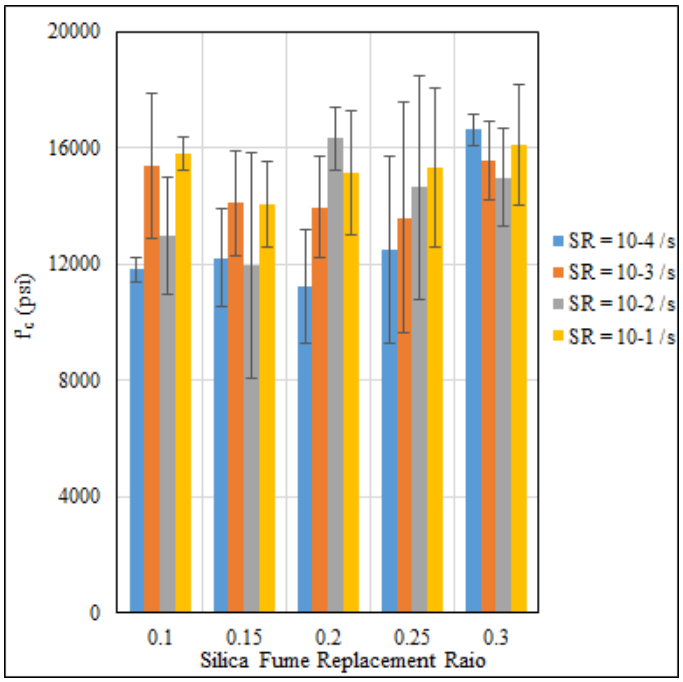

Figure 4.2: Variation of average compressive strength with silica fume replacement ratio for HSCM with constant paste volume

used to cast the specimens for constant paste volume mixes. The sand is sieved down to 0.0117-inch particle size (#50 sieve). The sand fraction is varied from 0.16 to 0.72 in five batches.

Although the variation of sand fraction is quite high, no discernable pattern of its effect on compressive strength is observed, as shown in Figure 4.3. A noticeable drop of strength is observed for sand fraction of 0.36. It is difficult to describe the reason for this drop, except attributing it to specimen preparation. Ignoring 0.36 sand fraction, a slight increase in strength with increasing sand fraction is observed, barring the lowest strain rate. Although, such behavior is reported for high strength concrete with coarse aggregate to projectile impact (Zhang et al. 2005), further studies are required to understand this trend for HSCM mix with fine aggregate only.

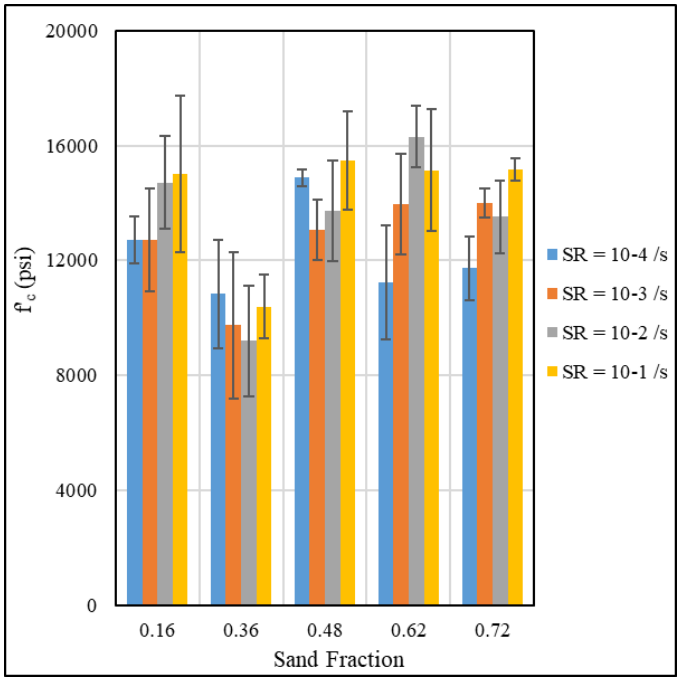

Figure 4.3: Variation of average compressive strength with sand fraction for HSCM with constant paste

Particle size plays a significant role to produce a compact mix and therefore high strength of HSCM mix. Effect of maximum particle size on compressive strength at different strain rate is presented in Figure 4.4. For the first part of this research program, 3 maximum particle sizes are considered. The first set of data presented in Figure 4.4 has all the particles passing #50 sieve (0.0117 inch). The second and third set of data have 50% particles passing #40 (0.0165 inch) and #30 (0.0234 inch) sieves, respectively, and 50% particles passing #50. sieve.

The strength of HSCM mixes is found to be higher or almost similar, ignoring few outliers. No definite conclusion is drawn and the range of particle size distribution should be increased to get a better picture. In later part of this thesis, the effect of gradation of industry grade quartz and silica sand is explored.

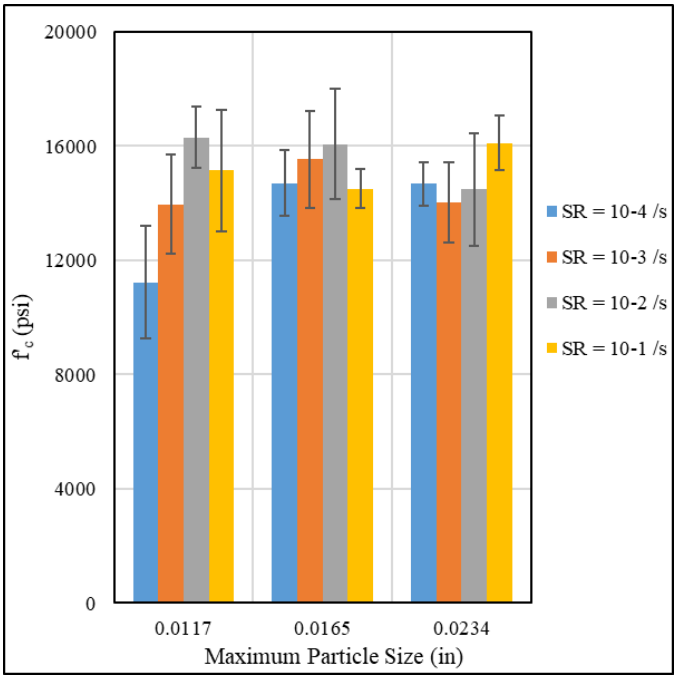

Figure 4.4: Variation of average compressive strength with maximum particle size for HSCM with constant paste volume

4.2.2 Impact Toughness

The full calculation of the results obtained from Charpy impact test, including standard deviation, are presented in Appendix C. A plot of the average values obtained is shown in Figures 4.5 and 4.6.

Impact energy absorption capacity decreases with increasing water-binder ratio, as shown in Figure 4.5. Although this pattern is evident for both upper and lower latch positions, specimens tested with upper latch position, i.e. higher impact velocity, show better energy absorption capacity for all specimens.

Combined with the compressive strength data presented in the previous section for same batches, it is concluded that lower water-binder ratio is preferred for higher strength and energy absorption capacity.

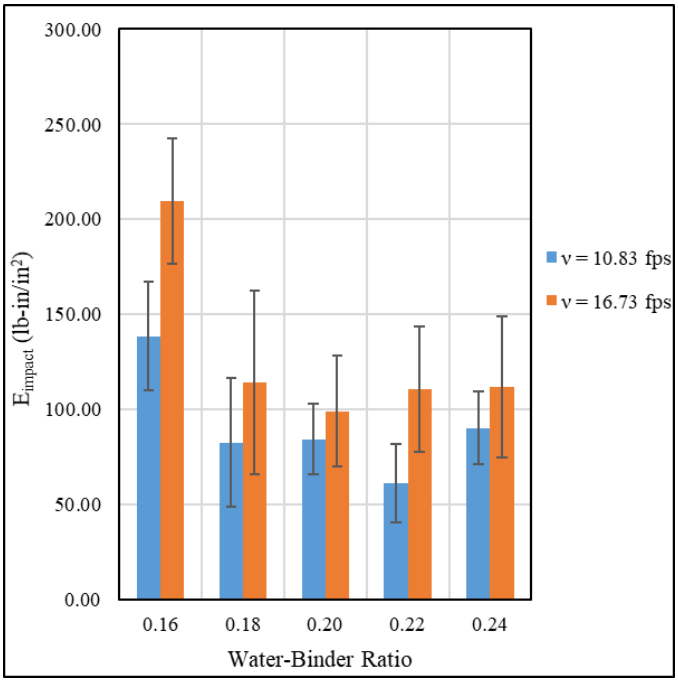

Figure 4.5: Variation of average impact toughness with water-binder ratio for HSCM with constant paste volume

Variation of impact energy absorption capacity with respect to increasing silica fume replacement, in Figure 4.6, also shows clear decreasing pattern initially. This is likely due to higher cement content of mixes which results in better hydration and hence better capacity. For the highest silica fume replacement, energy absorption capacity again increases. One possible explanation is that the reaction between cement and silica fume activated at higher temperature creates C-S-H crystals providing better energy absorption. To confirm the presence of such crystals, chemical analysis of the matrix is required.

Although, without microstructural investigation, this conclusion should not be fully reached. More tests need to be conducted for higher silica fume percentage to discard any possibility that this result might be just a discrepancy. Again, higher energy absorption capacity is found for higher impact velocity.

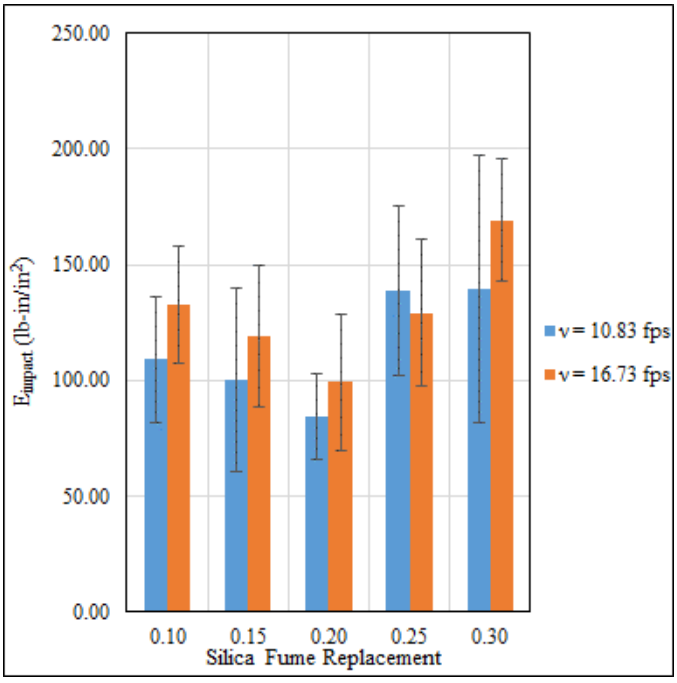

Figure 4.6:Variation of average impact toughness with silica fume ratio for HSCM with constant paste volume

Variation of impact energy absorption capacity for different sand fractions are presented in Figure 4.7. Energy absorption capacity also decreases with increasing sand fraction. This finding can be attributed to increasing non-homogeneity resulting from relatively large sand particles. Although, it increases again for highest sand fraction. This observation is also supported by the observation made in Figure 4.8, which illustrates the effect of maximum particle size on impact energy absorption capacity, showing increasing particle size increased energy absorption performance.

For Charpy test, information on standard deviation and coefficient of variation is scant in literature. Statistical information on drop-weight test is more available which shows high coefficient of variation in range of 40-55% (Song et al. 2005). This indicates that the high standard deviation in this research is not unexpected.

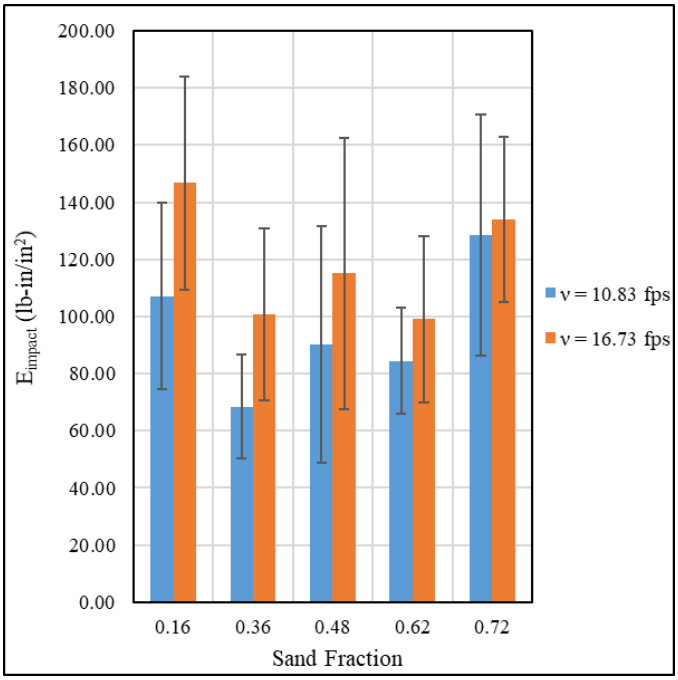

Figure 4.7:Variation of average impact toughness with sand fraction for HSCM with constant paste volume

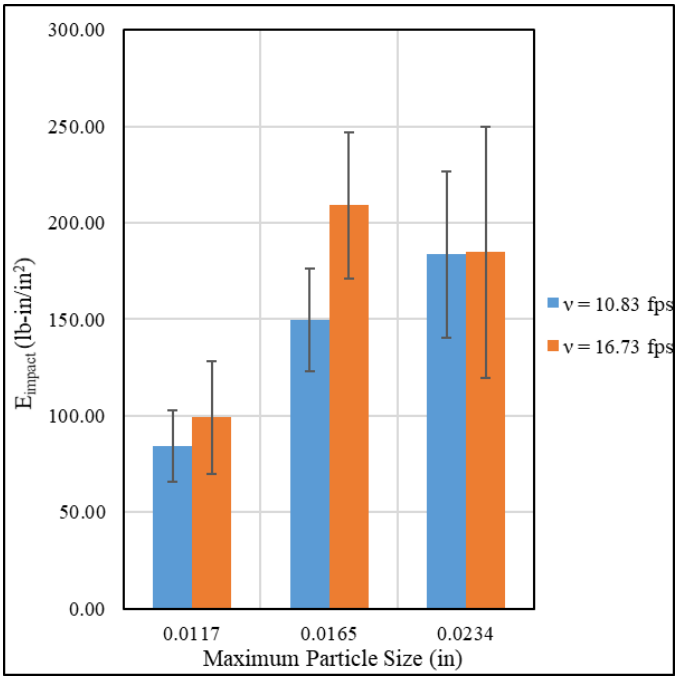

Figure 4.8: Variation of average impact toughness with maximum particle size for HSCM with constant paste volume

4.2.3 Compressive Strength and Impact Toughness

In this subsection, a relationship between compressive strength of HSCM mix and impact energy absorption capacity is sought. Previous research shows that the compressive toughness and impact toughness is linear-logarithmically related (Marar et al. 2001).

The regression analysis is performed by linearizing the impact toughness data and applying the set of equations show from Equations (4.2) to (4.6).

$$y = A + Bln(x) \tag{4.1}$$

$$B = \frac{S_{xy}}{S_{xx}} \tag{4.2}$$

$$A = \bar{y} - B\,\overline{\ln(x)} \tag{4.3}$$

$$S_{xx} = \frac{\sum(lnx_i)^2}{n} - \overline{\ln(x)}^2 \tag{4.4}$$

$$S_{yy} = \frac{\sum(\ln(x_i) \times y_i}{n} - \overline{\ln(x)} \times \bar{y} \tag{4.5}$$

Although, in this section, the compressive toughness is not calculated, following the research mentioned in this paragraph, a relationship between compressive strength at various strain rates and impact energy absorption capacity at two different impact velocity is pursued, and presented in Figure 4.9 and 4.10. Equations 4.7 to 4.10 shows the linear logarithmic relationships between compressive strength and normalized impact toughness for impact velocity of 10.83 fps.

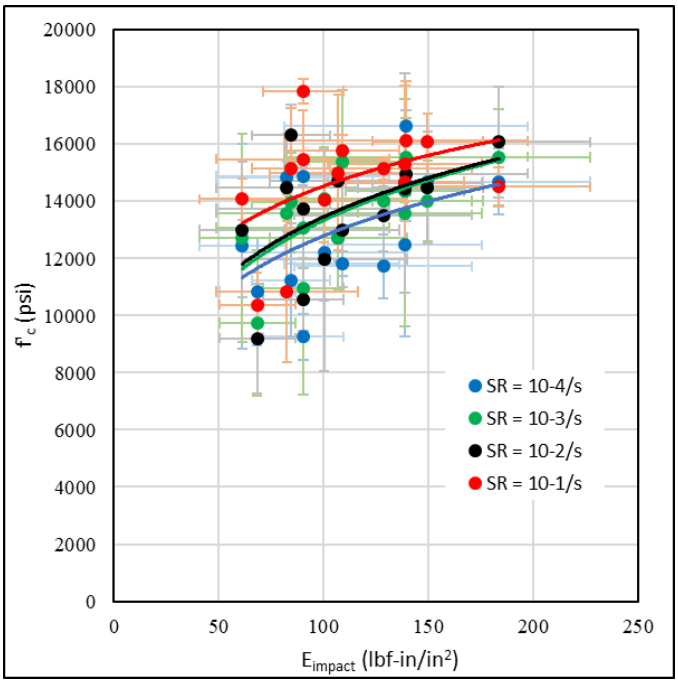

Figure 4.9: Relationship between compressive strength and impact toughness for HSCM with constant paste volume (v = 10.83 fps)

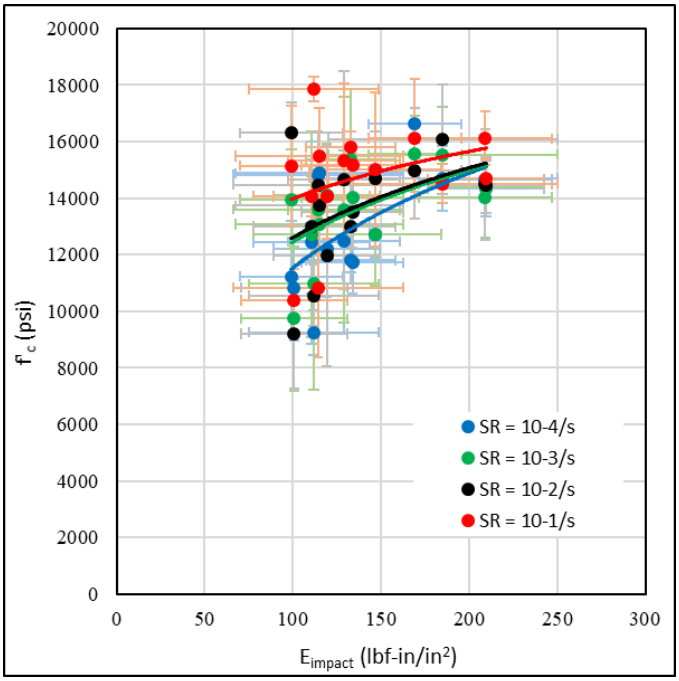

Figure 4.10: Relationship between compressive strength and impact toughness for HSCM with constant paste volume (v = 16.73 fps)

$$f_c' = 2976.4\ln(E_{impact}) - 916.52, \quad \dot{\varepsilon} = 10^{-4}\ s^{-1} \qquad (4.6)$$

$$f_c' = 3461.2\ln(E_{impact}) - 2607.9, \quad \dot{\varepsilon} = 10^{-3}\ s^{-1} \qquad (4.7)$$

$$f_c' = 3360.2\ln(E_{impact}) - 2017.7, \quad \dot{\varepsilon} = 10^{-2}\ s^{-1} \qquad (4.8)$$

$$f_c' = 2657.1\ln(E_{impact}) - 2295.1, \quad \dot{\varepsilon} = 10^{-1}\ s^{-1} \qquad (4.9)$$

Similarly, equations 4.11 to 4.14 shows the linear logarithmic relationship between those parameters for impact velocity of 16.73 fps (high latch position). In these equations, f_c' is the 28-days compressive strength of HSCM cubes in *psi* and E_{impact} is the impact toughness normalized with respect to the cross section of failure plane of HSCM specimen found by Charpy impact test in *in-lb/in*^{2}.

$$f_c' = 4829\ln(E_{impact}) - 10703, \quad \dot{\varepsilon} = 10^{-4}\ s^{-1} \tag{4.10}$$

$$f_c' = 3645.8\ln(E_{impact}) - 4327.2, \quad \dot{\varepsilon} = 10^{-3}\ s^{-1} \tag{4.11}$$

$$f_c' = 3551.8\ln(E_{impact}) - 3747.3, \quad \dot{\varepsilon} = 10^{-2}\ s^{-1} \tag{4.12}$$

$$f_c' = 2414.5\ln(E_{impact}) - 2860.1, \quad \dot{\varepsilon} = 10^{-1}\ s^{-1} \tag{4.13}$$

Coefficient of correlation, r, is also calculated using the relationship shown in Equation 4.15. |r| values are plotted in Figure 4.11. In general, |r| reduced with increasing strain rates. Moreover, |r| values mostly vary between 0.3 to 0.7, implying moderate correlation in data set.

$$r = \frac{S_{xy}}{\sqrt{S_{xx}} \times \sqrt{S_{yy}}} \tag{4.14}$$

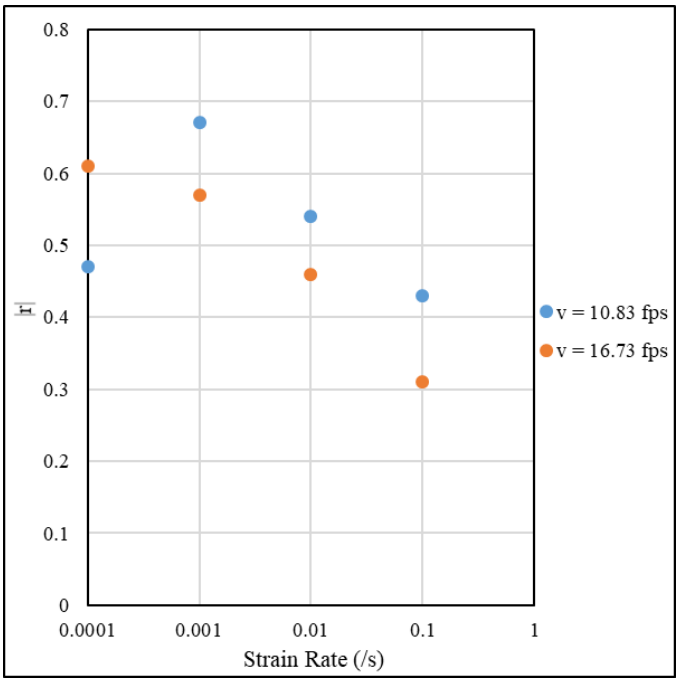

Figure 4.11: Variation of correlation coefficient with strain rate for compressive strength and impact toughness HSCM mix with constant past volume

4.3 HSCM Mix with Quartz and Silica Sand

As previously mentioned, the primary focus of this research program is to find a mix which can be classified as UHPC and then characterize its behavior under high frequency dynamic shear loading. It is obvious from previous section that this goal is not met. Therefore, the research program is redesigned to investigate the contribution of individual components to optimize the mix. With this goal and working on the assumption that the local sand used in the initial mixes is not good enough, industrial grade high quality fine quartz and silica sands are procured from two different suppliers, namely Granusil and US Silica. These sands are used to prepare the HSCM mixes described in rest of the sections of this chapter.

4.3.1 Effect of Gradation

The gradations of the sands are determined by using Malvern Mastersizer 2000 laser particle size analyzer from the Geology department of Utah State University. Generally, for concrete mixes, fineness modulus of aggregate is measured and reported. But in this research, instead of fineness modulus, coefficient of uniformity (C_u) is reported from the gradation curve presented in Appendix A. The particle size in sand samples are so small that the standard ASTM sieve cannot fully capture the particle size distribution of these samples. This is the underlying reasoning for omitting fineness modulus. C_u is frequently used by engineers to classify fine grained sands and soils (Craig 2004), and defined in Equation 4.16:

$$C_u = \frac{D_{60}}{D_{10}} \qquad (4.15)$$

Where,

$$D_x = Diameter\ of\ the\ particles\ for\ which\ x\%\ of\ the\ particles\ are\ finer$$

Figure 4.12 presents compressive strength versus coefficient of uniformity plot. Higher the value of C_u, the larger the range of particle sizes in the sample. The plot demonstrates that, with larger particle size distribution, the strength of the mix improves. It can be inferred that a wide range of particle size distribution of the fine sand is warranted to get a high strength mix. The wide range of fine particles effectively fill the voids of the mix, resulting a denser matrix and hence higher strength. Another notable finding is fine quartz sand performs better than silica sand.

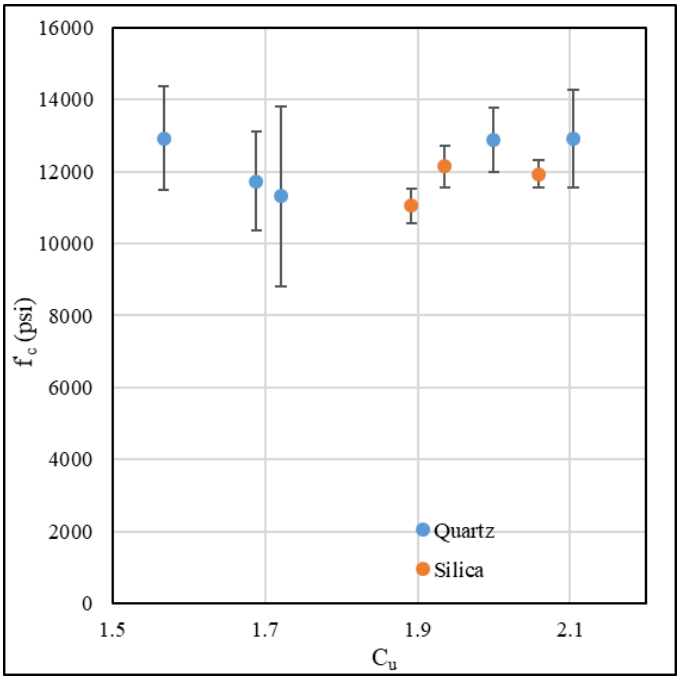

Figure 4.12: Variation of average compressive strength with coefficient of uniformity

4.3.2 Effect of Sand Fraction

To evaluate the effect of sand fraction, four sand fraction have been considered (0.36, 0.62, 0.77, and 0.92). The sands are sieved down to particle size passing #50 sieve. Compressive strength is determined according to ASTM C 39 standard. Sand fraction and compressive strength data are plotted in Figure 4.13. The plot shows that with increasing sand fraction, the compressive strength generally decreases. This trend can be attributed to the reduced density of HSCM matrix due to higher non-homogeneity resulting from higher sand fraction.

Compressive strength significantly improves compared to the data shown in Figure 4.12, which is obtained with mixes with un-sieved, larger sand samples. This implies that smaller sand particles are better to achieve higher strength. A wider range of sand fraction should be used to find an optimum level.

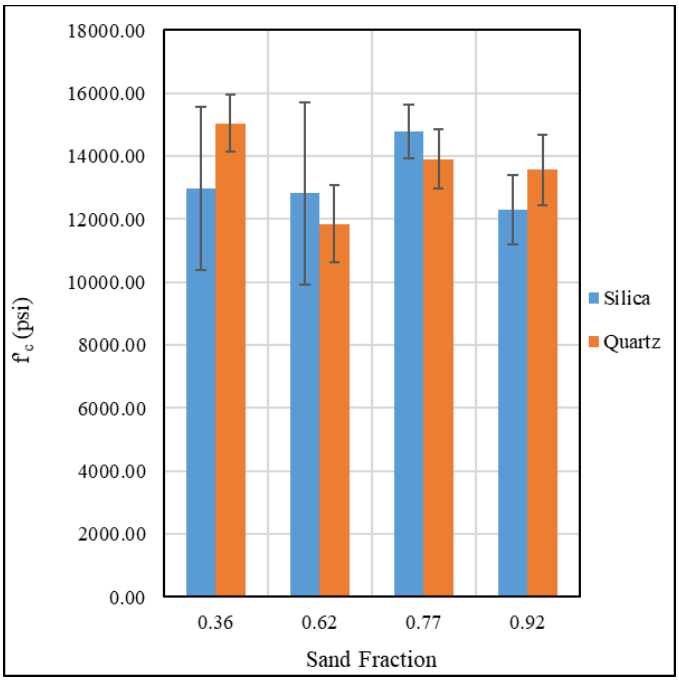

Figure 4.13: Variation of average compressive strength with sand fraction

The difference in compressive strength between the quartz and silica sands becomes insignificant, if not diminishes, for this mix when compared to Figure 4.12. The mixes in Figure 4.13 have larger sand particles. It can be inferred that when finer particle sizes are used for HSCM mix, the effect of sand type plays less significant role, therefore, it may be possible to use regular local sand with very fine sand particles reducing the cost of HSCM.

Variation of impact energy absorption capacity with sand fractions are plotted in Figures 4-14 and 4-15. for two different impact velocity is. Unlike compressive strength, impact energy absorption capacity shows opposite trend. Highest impact toughness is achieved for highest sand fraction. As before, the material appears to perform better under impact load for higher impact velocity.

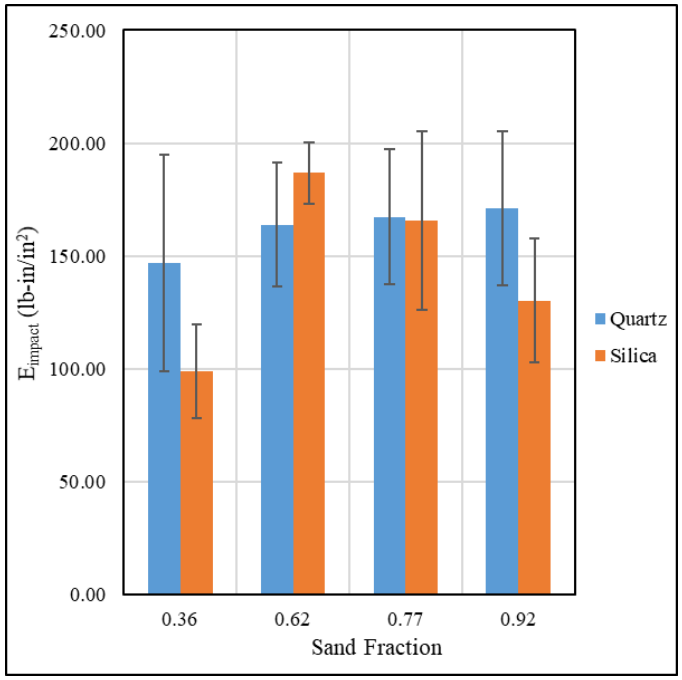

Figure 4.14: Variation of average impact toughness and sand fraction (v = 16.73 fps)

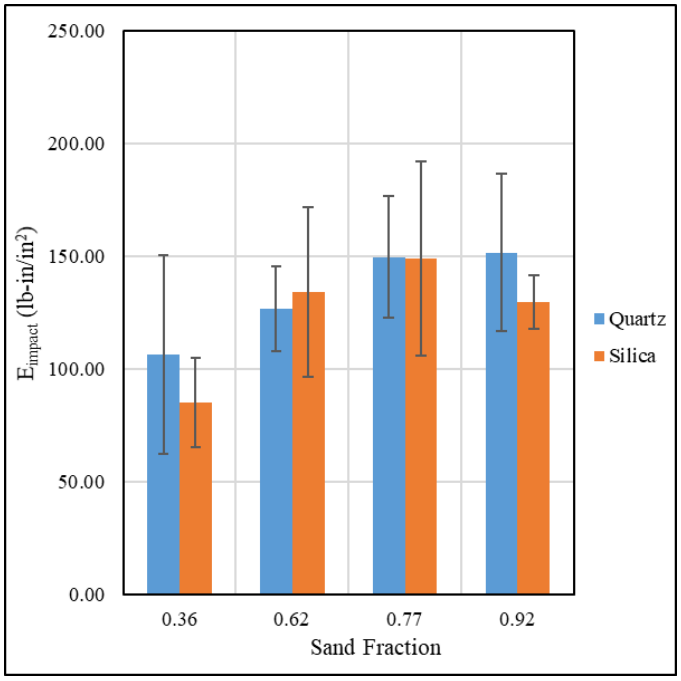

Figure 4.15: Variation of average impact toughness and sand fraction (v = 10.83 fps)

4.4 Compressive Strength, Compressive Toughness, and Impact Toughness

A relationship between compressive strength and impact toughness is sought. Specimens are tested for compressive strength for four strain rates. Additionally, compressive toughness up to peak load, calculated by numerical integration of the area under the load-deflection curves and normalized with respect to the volume of each specimen, is plotted against normalized impact toughness to correlate these two parameters in Figures 4-16 to 4-19.

28-day compressive strength vs. normalized impact toughness and normalized compressive toughness vs. normalized impact toughness data are fitted in liner-logarithmic lines. The equations for these fitted lines are found using Equations 4.2 to 4.6.

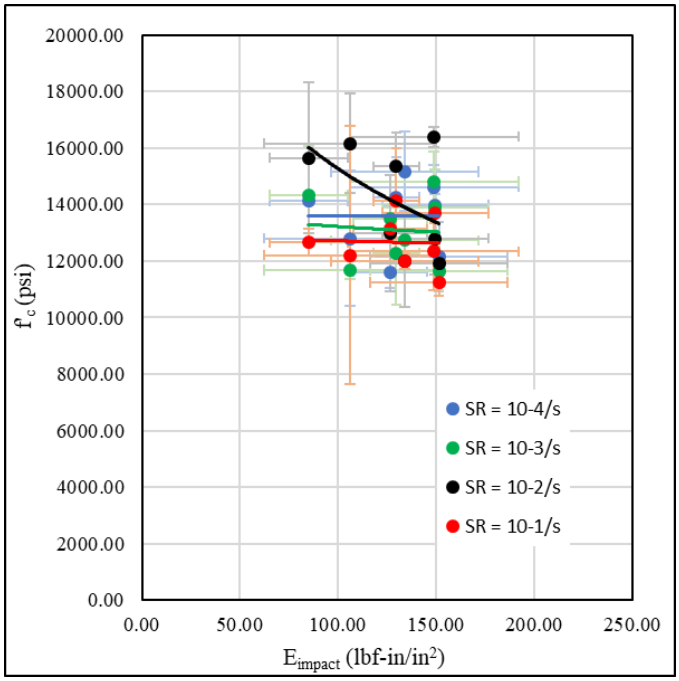

Figure 4.16: Relationship between average compressive strength and average impact toughness for HSCM with quartz and silica sand (v = 10.83 fps)

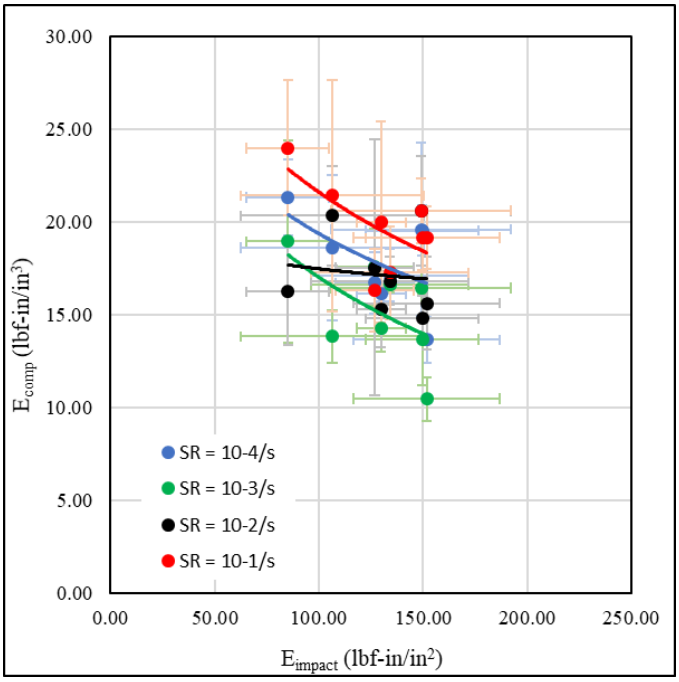

Figure 4.17: Relationship between average compressive toughness and average impact toughness for HSCM with quartz and silica sand (v = 10.83 fps)

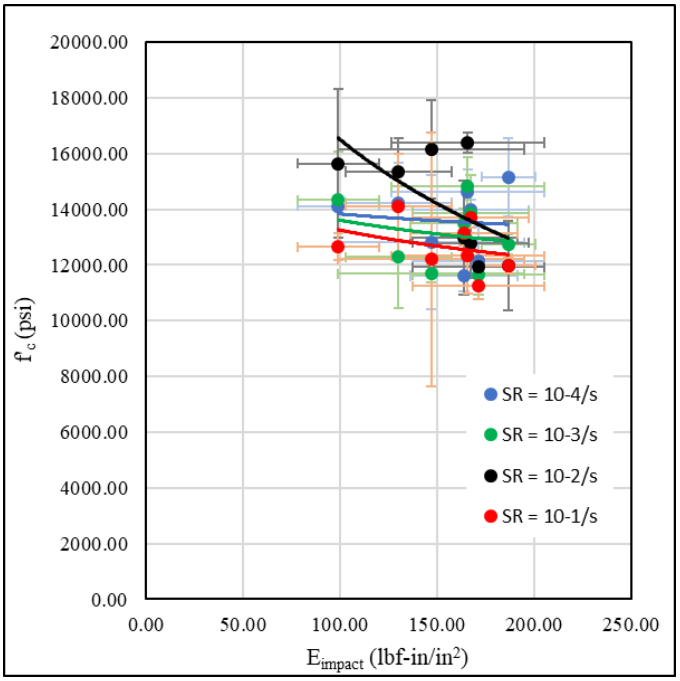

Figure 4.18: Relationship between average compressive strength and average impact toughness for HSCM with quartz and silica sand (v = 16.73 fps)

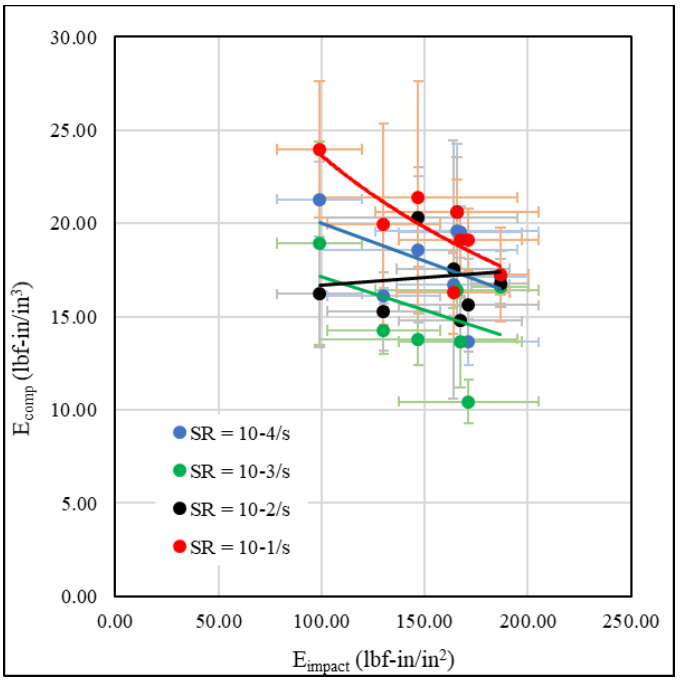

Figure 4.19: Relationship between average compressive toughness and impact toughness for HSCM with quartz and silica sand (v = 16.73 fps)

Equations 4.17 to 4.20 are for lower impact velocity of 10.83 fps and Equations 4.21 to 4.24 are for higher impact velocity of 16.73 fps. These equations are the relationships between 28-days compressive strength of cubes and impact toughness.

$$f_c' = 2.8268\ln(E_{impact}) + 13569, \quad \dot{\varepsilon} = 10^{-4}\ s^{-1} \tag{4.16}$$

$$f_c' = -477.2\ln(E_{impact}) + 15416, \quad \dot{\varepsilon} = 10^{-3}\ s^{-1} \tag{4.17}$$

$$f_c' = -4675\ln(E_{impact}) + 36800, \quad \dot{\varepsilon} = 10^{-2}\ s^{-1} \tag{4.18}$$

$$f_c' = -200\ln(E_{impact}) + 13635, \quad \dot{\varepsilon} = 10^{-1}\ s^{-1} \tag{4.19}$$

$$f_c' = -600.8\ln(E_{impact}) + 16598, \quad \dot{\varepsilon} = 10^{-4}\ s^{-1} \tag{4.20}$$

$$f_c' = -477.2\ln(E_{impact}) + 15416, \quad \dot{\varepsilon} = 10^{-3}\ s^{-1} \tag{4.21}$$

$$f_c' = -5670\ln(E_{impact}) + 42613, \quad \dot{\varepsilon} = 10^{-2}\ s^{-1} \tag{4.22}$$

$$f_c' = -1414\ln(E_{impact}) + 19766, \quad \dot{\varepsilon} = 10^{-1}\ s^{-1} \tag{4.23}$$

Equations 4.25 to 4.28 are the relationships between compressive toughness, E_{comp}, and impact toughness at the impact velocity of 10.83 fps. The unit of compressive toughness is in-lb/in^3.

$$E_{comp} = -6.42\ln(E_{impact}) + 48.91, \quad \dot{\varepsilon} = 10^{-4}\ s^{-1} \tag{4.24}$$

$$E_{comp} = -7.52\ln(E_{impact}) + 51.64, \quad \dot{\varepsilon} = 10^{-3}\ s^{-1} \tag{4.25}$$

$$E_{comp} = -1.31\ln(E_{impact}) + 23.47, \quad \dot{\varepsilon} = 10^{-2}\ s^{-1} \tag{4.26}$$

$$E_{comp} = -7.834\ln(E_{impact}) + 57.66, \quad \dot{\varepsilon} = 10^{-1}\ s^{-1} \tag{4.27}$$

Similarly, for higher impact velocity of 16.73 fps, Equations 4.29 to 4.32 shows the linear-logarithmic relationship between compression toughness and impact toughness.

$$E_{comp} = -5.80 \ln(E_{impact}) + 46.94, \quad \dot{\varepsilon} = 10^{-4}\ s^{-1} \qquad (4.28)$$

$$E_{comp} = -5.39 \ln(E_{impact}) + 42.26, \quad \dot{\varepsilon} = 10^{-3}\ s^{-1} \qquad (4.29)$$

$$E_{comp} = -1.47 \ln(E_{impact}) + 9.78, \quad \dot{\varepsilon} = 10^{-2}\ s^{-1} \qquad (4.30)$$

$$E_{comp} = -9.50 \ln(E_{impact}) + 67.41, \quad \dot{\varepsilon} = 10^{-1}\ s^{-1} \qquad (4.31)$$

Figure 4.20 presents that the correlation coefficient is very scattered with no discernable pattern for the specimens discussed in the current section, unlike as shown in Figure 4.11. This plot also shows that the correlation in data set ranges, mostly, from weak to no correlation.

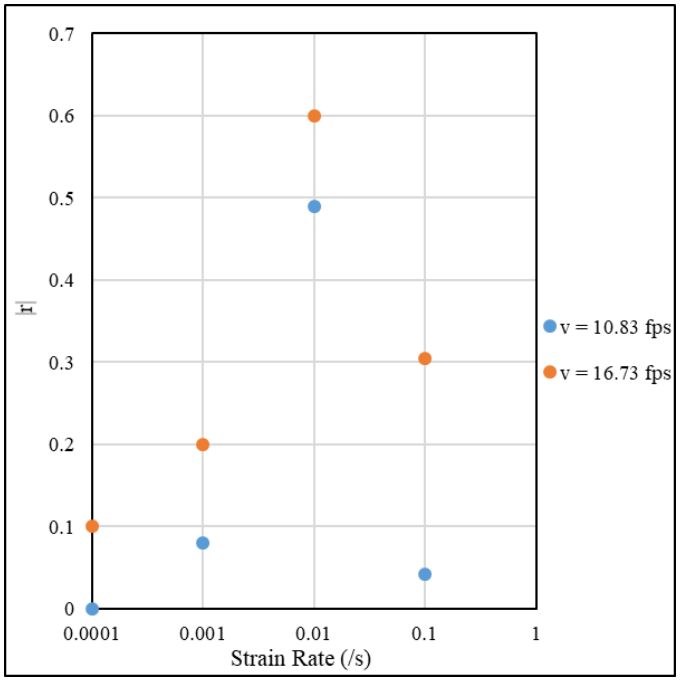

Figure 4.20: Variation of correlation coefficient with strain rate for average compressive strength and impact toughness of HSCM mix with quartz and silica sand

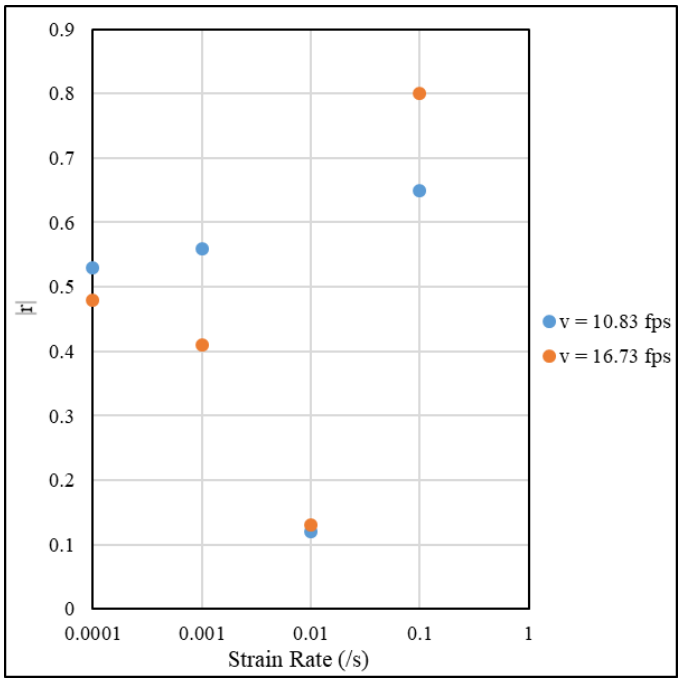

Figure 4.21: Variation of correlation coefficient with strain rate for compressive toughness and impact toughness of HSCM mix with quartz and silica sand

Variation of correlation coefficient with strain rate for compressive toughness and impact toughness of HSCM mix with quartz and silica sand is presented in Figure 4.21. This plot implies that, generally, the correlation between compressive and impact toughness is stronger compared to compressive strength and impact toughness.

4.5 Summary

From analysis of the experimental data, overall conclusions on compressive strength, energy absorption, contribution of constituents are made. The results and conclusions, detailed in previous sections of this chapter, are summarized in subsequent subsections.

4.5.1 Compressive Strength

Maximum compressive strength for HSCM cubes with constant paste volume, across all strain rate barring the maximum, are achieved for water-to-binder ratio of 0.2, indicating the optimum ratio. The anomaly observed for the highest strain rate seems to be an outlier. At the highest strain rate, the relatively small specimen fails very quickly, giving the UTM almost no time to operate at a constant rate. This seems be the source of error at the highest strain rate. Testing larger specimen should solve this problem. From the test results, no definite relationship between compressive strength and silica fume replacement is interpreted, which can be attributed to the scatter of the experimental data. A slight increase in strength with increasing sand fraction, for higher strain rate, is observed, although large scatter and a drop of strength for 0.36 sand fraction prevent from drawing any conclusion. More tests are required to capture the behavior comprehensively. No conclusion on the effect of particle size is drawn either.

The test results achieved from batches made with quartz and silica sands indicates that a wide range of particle size is warranted for high strength of HSCM mix. Unlike the results from constant paste volume mixes, it is concluded that lower sand fractions and smaller particle size are better to get higher compressive strength.

4.5.2 Impact Toughness

For constant paste volume mixes, normalized impact energy absorption capacity or impact toughness decreases with increasing water-binder ratio. But for increasing silica fume replacement, impact toughness decreases initially and then peak for the highest silica fume ratio. Impact energy absorption capacity increase with decreasing

sand fraction. At higher impact velocity, these mixes are found to perform better regarding impact energy absorption.

Test results for HSCM mix with quartz and silica sand demonstrate that higher sand fractions result in higher impact energy absorption capacity.

4.5.3 Compressive Strength vs. Impact Toughness

A relationship between compressive strength and impact toughness is found and coefficient of correlation is determined for different strain rates. In general, for HSCM mix with constant paste volume, the correlation coefficient decreases for higher strain rates. The correlation coefficient indicates moderate correlation in the data set. For mixes with quartz and silica sands, no such discernable pattern for correlation coefficient is observed. Although, when impact toughness is related to compressive toughness, instead of compressive strength, higher correlation is observed. More test results are required to reduce the standard deviation, which should result in a better picture of these trends.

CHAPTER 5

CONCLUSION AND FUTURE WORK

5.1 Summary and Conclusion

This chapter summarizes the methodology used for this research program as well as the results and conclusions from experimental program. Possible direction from future research work is also discussed.

5.1.1 Methodology Summary

To accomplish the research objectives, specimen preparation and laboratory testing is undertaken according to ASTM standards. There are instances where the ASTM standard for normal concrete cannot be followed for HSCM mixes. In those instances, modification of the standards based on existing ASTM standards, available literature, and engineering judgement is made.

The mix design used is based on a previous research by Thomas et al. (2017), which followed the mix design presented by Allena and Newtson (2010). These mix proportions and curing treatments are designed to produce Ultra High Performance Concrete. Although the strength requirement for UHPC could not be achieved, this research helps to quantify the contribution of individual components of commonly used UHPC mixture components to compressive strength at different strain rates of loading and dynamic shear energy absorption capacity.

Ordinary Portland cement conforming to ASTM C 150-15 standard specification for type II-V, dry densified silica fume supplied by BSAF conforming to ASTM C 1240-

15, high range water reducing admixture MasterGlenium 3030 conforming to ASTM C 494/C494M-17, and three types of fine sands are used to make different batches in a parametric study.

The preliminary objective of this research, as discussed in Chapter 1, is not met as the required compressive strength for HSCM mixes with constant paste volume of 18 ksi is not achieved with locally available sand. However, the research did provide insight into the contribution of the mixture components to the compressive strength and dynamic shear energy absorption capacity. These two parameters are analyzed to determine if a relationship can be determined.

Based on the shortcomings of the preliminary objective, the research concentrated on the effect of fine sands on the compressive strength of the mix tested at different strain rates (10^{-4}, 10^{-3}, 10^{-2}, and 10^{-1} per second). Commercially available crushed quartz and silica sands are procured in the second phase of testing. The particle size distribution of these sands are obtained using a laser particle size analyzer. This data is used to investigate research objective 1 of phase two as mentioned in Chapter 1. Parametric studies on the effect of sand fractions are evaluated to meet objective 2, where compressive strength, compressive toughness, and impact toughness by testing Charpy specimens are determined. In conjunction with objective 2, this data is analyzed to meet objectives 3 and 4.

5.1.2 Result Summary

The test results from the experiments are processed, analyzed and then the trends are observed to achieve the objectives of this research program. From the results, it is

clear that compressive strength for constant paste volume mixes decreases with increasing water-binder ratio. Despite some anomaly in test results, a range of 0.16 to 0.2 water-binder ratio seems optimum to achieve higher compressive strength. A similar trend is observed for impact toughness. Based on these two observations, it can be inferred that the optimum water-binder ratio for HSCM mix with constant paste volume is 0.16. Optimum silica fume ratio of these mixes is found to be 0.2 for compressive strength. No such conclusion is reached for impact energy absorption capacity, and as such, more research is suggested to gain a clearer understanding. For sand fractions and maximum particle size, no definite conclusion of their effect on compressive strength is drawn. Impact energy absorption capacity is found to decrease with increasing sand fraction, possibly due to higher non-homogeneity of the mix. But it increases again at the highest fraction. Larger particle size also improves impact energy absorption performance of HSCM mix. Although, a wide range of particle size and sand fraction should be investigated to confirm this finding.

When a correlation between compressive strength at different strain rates and dynamic impact energy absorption capacity is studied, good correlation between these two parameters are observed for lower strain rates and then the correlation decreases as the strain rates increases. The correlation coefficient is found to be as much as 67% for a strain rate of 0.001 s^{-1}. Better correlation is found for lower impact velocity.

In the second phase of the research program, silica and crushed quartz sands are used. By using a laser particle size analyzer, coefficient of uniformity, C_u, is calculated. C_u is higher when the particle size range is wider in the sand samples. It is inferred from

the test data that a wider range of particle size distribution is better for achieving higher strength, which results in more homogeneity and fewer voids in the matrix. To evaluate the effect of sand fraction in these batches, both silica and quartz sand samples are sieved down so that only those passing the #50 sieve are used. Four sand fractions are considered and it is concluded that lower sand fractions result in higher compressive strength. Interestingly, an opposite trend is observed for impact energy absorption capacity, where the capacity increases with increased sand fraction. Zhang et al. showed that, for high strength concrete subjected to projectile impact, impact resistance increases with increasing coarse aggregate content, as long as workability of concrete is not compromised (Zhang et al., 2005). Existing literatures do not explore much on the impact resistance of high strength concretes with only fine sands and different sand fraction. More studies are recommended to fully understand the mechanism of this behavior of HSCM mix.

Finally, correlations between compressive strength and impact toughness as well as correlation between compressive toughness and impact toughness is sought. Compressive toughness is calculated by numerical integration of the load-deflection curve of the HSCM cubes and then normalized with respect to volume of the cube. Correlation coefficients indicates that better correlation is achieved for compressive toughness and impact toughness.

The test results show high standard deviations. This can be attributed to many factors, such as, the size of the test specimens for both compressive strength and Charpy specimens, variability in lab condition during specimen preparation and curing, and

quality of materials. This research program acknowledges that some of the trends observed from test results are inconclusive and warrants more testing and better control in laboratory environment.

5.2 Future Direction

The long term goal of this research program is to produce low-cost ultra-high performance concrete with locally available material, characterization of its mechanical properties, isolation of the contribution of individual components of the material, analyzing its behavior under dynamic shear loading, establishing relationships between compressive strength and compressive toughness or impact toughness, and evaluating its structural performance. As an initial attempt, a high strength mix is produced and parametric studies are conducted.

High variability in test results indicates that, in the future, the primary goal should be set to reduce the standard deviation of the results. One source of the variability is the smaller sample size. At the inception of this research, no standard for producing and testing UHPC was available. ASTM C1856 / C1856M-17, Standard Practice for Fabricating and Testing Specimens of Ultra-High Performance Concrete, was published when the laboratory testing was ongoing. Among other things, the standard requires 3 inch by 6 inch cylindrical specimens for compressive strength test whereas the research in this study utilizes 2 inch cubes. In the future, the test sample should conform to the specification, which should reduce the standard deviation of compressive test results because of larger specimen size. For impact energy absorption capacity tests, no standard for Charpy test is available for compendious material. In absence of standard, ASTM

E23, Standard Test Methods for Notched Bar Impact Testing of Metallic Materials was modified for this program. The small size of impact test specimens possibly contributes to the higher standard deviation, as well. There are other impact test methods for concrete can be found in literatures, such as, the drop-weight and modified drop-weight test (Badr and Ashour 2005; Barr and Bouamrata 1988). In future, these tests can be performed in conjunction with Charpy test.

The necessity of a wider range of parametric study is felt, especially to capture the full impact absorption behavior of the material. The test results indicate that, while compressive strength is improved by smaller particle size resulting in a more compact, denser matrix, impact energy may be improved by using slightly larger sand particles. Also, the effect of particle size distribution should be analyzed by employing custom gradation. A wider range of sand fractions should also be studied to find the optimum dosage of this parameter so that compression and impact performance of the material can be achieved. Similarly, the effect of silica fume, especially at different temperatures and curing regimes is another area worth more exploration. Existing literatures shows that weaker CH crystal may not be found in UHPC, while elevated temperature and addition of silica fume create stronger C-S-H crystals and thus provided excellent mechanical properties (Reda et al. 1999). In light of these findings, extensive chemical and mineralogical analysis along with microscopic image analysis is recommended for future studies on HSCM mixes and improvement of the material so that UHPC can be produced at a lower cost. To fully characterize this material, tensile testing, fracture testing, penetration resistance testing, shrinkage testing, creep testing, thermal expansion testing,

durability testing should also be performed. Addition of fibers to improve the tensile, flexural, and impact performance of HSCM is another significant area for future study.

Practical design parameters and equations cannot be developed using only mechanical property evaluation. Therefore, laboratory testing on full scale structural components as well as numerical modeling of those systems with finite-element based software should be performed; especially for extreme loading event such as impact, blast, and environmental loading such as earthquake and hurricane.

REFERENCES

Alkaysi, M., El-Tawil, S., Liu, Z., and Hansen, W. (2016). “Effects of silica powder and cement type on durability of ultra high performance concrete (UHPC).” *Cement and Concrete Composites*, Elsevier, 66, 47–56.

Allena, S., and Newtson, C. M. (2011). “Ultra-high strength concrete mixtures using local materials.” *Journal of Civil Engineering and Architecture*, David Publishing Company, 1840 Industrial Drive Suite 160 Libertyville …, 5(4), 322–330.

ASTM. (2014). “ASTM C469 / C469M -14: Standard Test Method for Static Modulus of Elasticity and Poisson’s Ratio of Concrete in Compression.” ASTM International, West Conshohocken, PA.

ASTM. (2015). “ASTM C 1240-15 Standard Specification for Silica Fume Used in Cementitious Mixtures.” ASTM International, West Conshohocken, PA.

ASTM. (2015). “ASTM C617 / C617M - 15, Standard Practice for Capping Cylindrical Concrete Specimens.” ASTM International, West Conshohocken, PA.

ASTM. (2015c). “ASTM C617 / C617M - 15, Standard Practice for Capping Cylindrical Concrete Specimens.” ASTM International, West Conshohocken, PA.

ASTM. (2016). “C39/C39M-14: Standard Test Method for Compressive Strength of Cylindrical Concrete Specimens.” ASTM International, West Conshohocken, PA.

ASTM. (2016). “ASTM C150-16, Standard Specification for Portland Cement.” *ASTM*, ASTM International, West Conshohocken, PA.

ASTM. (2017). “ASTM C494 / C494M - 17, Standard Specification for Chemical Admixtures for Concrete.” ASTM International, West Conshohocken, PA.

ASTM. (2017). “ASTM C1856 / C1856M - 17, Standard Practice for Fabricating and Testing Specimens of Ultra-High Performance Concrete.” ASTM International, West Conshohocken, PA.

ASTM. (2018). “ASTM C192 / C192M - 18, Standard Practice for Making and Curing Concrete Test Specimens in the Laboratory.” ASTM International, West Conshohocken, PA.

ASTM. (2018). “ASTM E23 - 18 Standard Test Methods for Notched Bar Impact Testing of Metallic Materials.” ASTM International, West Conshohocken, PA.

Badr, A., and Ashour, A. F. (2005). “Modified ACI Drop-Weight Impact Test for Concrete.” *ACI Materials Journal*, 102(4), 249–255.

Barr, B., and Bouamrata, A. (1988). “Development of a repeated dropweight impact testing apparatus for studying fibre reinforced concrete materials.” *Composites*, Elsevier, 19(6), 453–466.

Chanvillard, G., Pimienta, P., Pineaud, A., and Rivillon, P. (1996). “Fatigue Flexural Behaviour of Pre-Cracked Specimens of Ductal® UHPFRC.” Lafarge.

Craig, R. F. (2004). *Craig’s Soil Mechanics, Seventh Edition*. Taylor & Francis.

Eide, M. B., and Hisdal, J.-M. (2012). “Ultra High Performance Fibre Reinforced Concrete (UHPFRC)–State of the art: FA 2 Competitive constructions: SP 2.2 Ductile high strength concrete.” SINTEF Building and Infrastructure.

Farnam, Y., Mohammadi, S., and Shekarchi, M. (2010). “Experimental and numerical investigations of low velocity impact behavior of high-performance fiber-reinforced cement based composite.” *International Journal of Impact Engineering*, Elsevier,

37(2), 220–229.

FHWA. (2018). “North American Deployments of UHPC in Highway Bridge Construction.”

Graybeal, B. A. (2006). *Material property characterization of ultra-high performance concrete*.

Graybeal, B., and Tanesi, J. (2007). “Durability of an ultrahigh-performance concrete.” *Journal of materials in civil engineering*, American Society of Civil Engineers, 19(10), 848–854.

Habel, K., Viviani, M., Denarié, E., and Brühwiler, E. (2006). “Development of the mechanical properties of an ultra-high performance fiber reinforced concrete (UHPFRC).” *Cement and Concrete Research*, Elsevier, 36(7), 1362–1370.

Hentz, S., Donzé, F. V, and Daudeville, L. (2004). “Discrete element modelling of concrete submitted to dynamic loading at high strain rates.” *Computers & structures*, Elsevier, 82(29–30), 2509–2524.

Ichikawa, S., Matsuzaki, H., Moustafa, A., ElGawady, M. A., and Kawashima, K. (2016). “Seismic-resistant bridge columns with ultrahigh-performance concrete segments.” *Journal of Bridge Engineering*, American Society of Civil Engineers, 21(9), 4016049.

de Larrard, F., and Sedran, T. (1994). “Optimization of ultra-high-performance concrete by the use of a packing model.” *Cement and Concrete Research*, Elsevier, 24(6), 997–1009.

Li, J., Wu, C., and Hao, H. (2015). “Residual loading capacity of ultra-high performance

concrete columns after blast loads." *International Journal of Protective Structures*.

Li, J., Wu, C., and Hao, H. (2015). "Investigation of ultra-high performance concrete slab and normal strength concrete slab under contact explosion." *Engineering Structures*, Elsevier, 102, 395–408.

Li, J., Wu, C., and Hao, H. (2015). "An experimental and numerical study of reinforced ultra-high performance concrete slabs under blast loads." *Materials & Design*, Elsevier, 82, 64–76.

Ma, J., Orgass, M., Dehn, F., Schmidt, D., and Tue, N. V. (2004). "Comparative investigations on ultra-high performance concrete with and without coarse aggregates." *Proceedings of international symposium on ultra high performance concrete, Germany*, 205–212.

Malvar, L. J., and Ross, C. A. (1998). "Review of strain rate effects for concrete in tension." *Materials Journal*, 95(6), 735–739.

Marar, K., Eren, Ö., and Celik, T. (2001). "Relationship between impact energy and compression toughness energy of high-strength fiber-reinforced concrete." *Materials letters*, Elsevier, 47(4–5), 297–304.

Millon, O., Riedel, W., Thoma, K., Fehling, E., and Nöldgen, M. (2009). "Fiber-reinforced ultra-high performance concrete under tensile loads." *9th International Conference on the Mechanical Behaviour of Materials under Dynamic Loading, DYMAT*, 671–677.

Nguyen, D. L., Ryu, G. S., Koh, K. T., and Kim, D. J. (2014). "Size and geometry dependent tensile behavior of ultra-high-performance fiber-reinforced concrete."

Composites Part B: Engineering, Elsevier, 58, 279–292.

Othman, H., and Marzouk, H. (2016). "Strain Rate Sensitivity of Fiber-Reinforced Cementitious Composites." *ACI Materials Journal*, 113(2), 143–150.

Othman, H., Marzouk, H., and Sherif, M. (2019). "Effects of variations in compressive strength and fibre content on dynamic properties of ultra-high performance fibre-reinforced concrete." *Construction and Building Materials*, Elsevier, 195, 547–556.

Park, J. K., Kim, S.-W., and Kim, D. J. (2017). "Matrix-strength-dependent strain-rate sensitivity of strain-hardening fiber-reinforced cementitious composites under tensile impact." *Composite Structures*, Elsevier, 162, 313–324.

Pyo, S., Wille, K., El-Tawil, S., and Naaman, A. E. (2015). "Strain rate dependent properties of ultra high performance fiber reinforced concrete (UHP-FRC) under tension." *Cement and Concrete Composites*, Elsevier, 56, 15–24.

Reda, M. M., Shrive, N. G., and Gillott, J. E. (1999). "Microstructural investigation of innovative UHPC." *Cement and Concrete Research*, Elsevier, 29(3), 323–329.

Richard, P., and Cheyrezy, M. (1995). "Composition of reactive powder concretes." *Cement and concrete research*, Elsevier, 25(7), 1501–1511.

Richard, P., and Cheyrezy, M. H. (1994). "Reactive powder concretes with high ductility and 200-800 MPa compressive strength." *Special Publication*, 144, 507–518.

Rossi, P. (2002). "Development of new cement composite materials for construction." *Innovations and Developments In Concrete Materials And Construction: Proceedings of the International Conference held at the University of Dundee, Scotland, UK on 9–11 September 2002*, Thomas Telford Publishing, 17–29.

Song, P. S., Wu, J. C., Hwang, S., and Sheu, B. C. (2005). “Assessment of statistical variations in impact resistance of high-strength concrete and high-strength steel fiber-reinforced concrete.” *Cement and Concrete Research*, Elsevier, 35(2), 393–399.

Sorensen, A. D., and Thomas, R. J. (2018). “Charpy Impact Test Methods for Cementitious Composites: Review and Commentary.” *Journal of Testing and Evaluation*, ASTM International, 46(6).

Sovják, R., Vavřiník, T., Máca, P., Zatloukal, J., Konvalinka, P., and Song, Y. (2013). “Experimental investigation of ultra-high performance fiber reinforced concrete slabs subjected to deformable projectile impact.” *Procedia Engineering*, Elsevier, 65, 120–125.

Terry Wipf, P. E., Sritharan, S., Abu-Hawash, A., Brent Phares, P. E., and Bierwagen, D. (2011). “Iowa’s ultra-high performance concrete implementation.” *RESEARCH news*.

Thomas, R. J., Bedke, C., and Sorensen, A. (2017). “Dynamic Shear Energy Absorption of Ultra-High Performance Concrete.” *World Academy of Science, Engineering and Technology, International Journal of Civil, Environmental, Structural, Construction and Architectural Engineering*, 11(3), 286–291.

Thomas, R. J., and Sorensen, A. D. (2017). “Review of strain rate effects for UHPC in tension.” *Construction and Building Materials*, Elsevier, 153, 846–856.

Wille, K., Naaman, A. E., El-Tawil, S., and Parra-Montesinos, G. J. (2012). “Ultra-high performance concrete and fiber reinforced concrete: achieving strength and ductility

without heat curing." *Materials and structures*, Springer, 45(3), 309–324.

Yalçınkaya, Ç., and Yazıcı, H. (2017). "Effects of ambient temperature and relative humidity on early-age shrinkage of UHPC with high-volume mineral admixtures." *Construction and Building Materials*, Elsevier, 144, 252–259.

Yi, N.-H., Kim, J.-H. J., Han, T.-S., Cho, Y.-G., and Lee, J. H. (2012). "Blast-resistant characteristics of ultra-high strength concrete and reactive powder concrete." *Construction and Building Materials*, Elsevier, 28(1), 694–707.

Yoo, D.-Y., Kang, S.-T., and Yoon, Y.-S. (2014). "Effect of fiber length and placement method on flexural behavior, tension-softening curve, and fiber distribution characteristics of UHPFRC." *Construction and Building Materials*, Elsevier, 64, 67–81.

Yoo, D.-Y., Lee, J.-H., and Yoon, Y.-S. (2013). "Effect of fiber content on mechanical and fracture properties of ultra high performance fiber reinforced cementitious composites." *Composite Structures*, Elsevier, 106, 742–753.

Yoo, D.-Y., Min, K.-H., Lee, J.-H., and Yoon, Y.-S. (2014). "Shrinkage and cracking of restrained ultra-high-performance fiber-reinforced concrete slabs at early age." *Construction and Building Materials*, Elsevier, 73, 357–365.

Yoo, D.-Y., and Yoon, Y.-S. (2015). "Structural performance of ultra-high-performance concrete beams with different steel fibers." *Engineering Structures*, Elsevier, 102, 409–423.

Zhang, F., Wu, C., Zhao, X.-L., Xiang, H., Li, Z.-X., Fang, Q., Liu, Z., Zhang, Y., Heidarpour, A., and Packer, J. A. (2016). "Experimental study of CFDST columns

infilled with UHPC under close-range blast loading." *International Journal of Impact Engineering*, Elsevier, 93, 184–195.

Zhang, M. H., Shim, V. P. W., Lu, G., and Chew, C. W. (2005). "Resistance of high-strength concrete to projectile impact." *International Journal of Impact Engineering*, Elsevier, 31(7), 825–841.

Zohrevand, P., and Mirmiran, A. (2011). "Cyclic behavior of hybrid columns made of ultra high performance concrete and fiber reinforced polymers." *Journal of Composites for Construction*, American Society of Civil Engineers, 16(1), 91–99.

APPENDICES

APPENDIX A. GRADATION CURVE FOR QUARTZ AND SILICA SAND

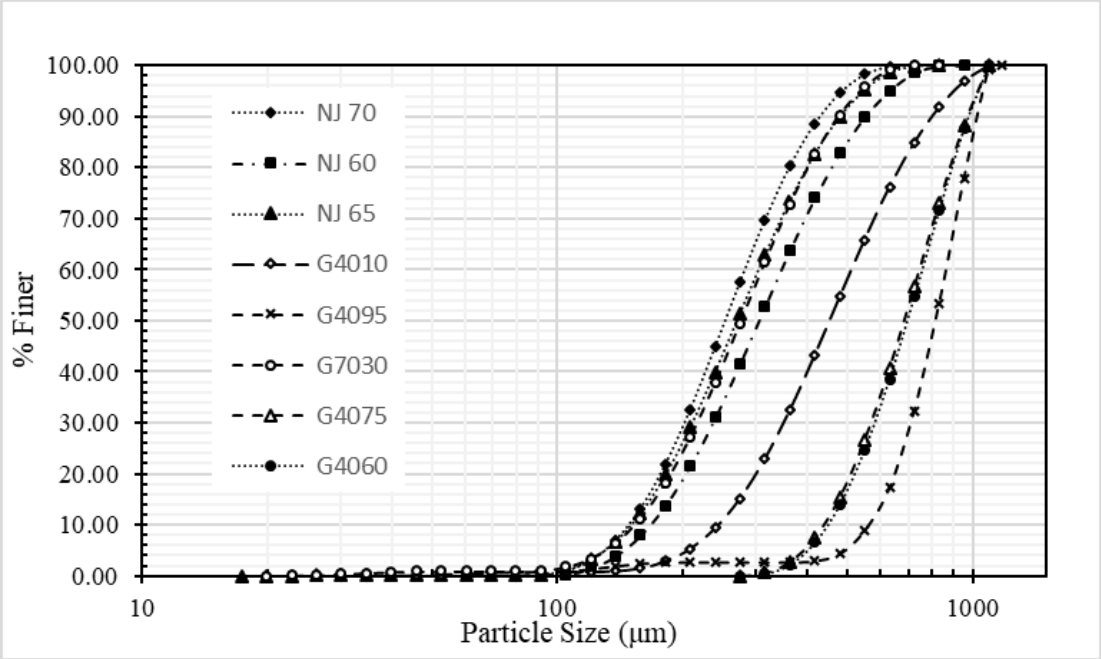

APPENDIX B. COMPRESSIVE TEST RESULTS FOR PHASE 1

Batch	Compressive Strength (psi)			
	Strain Rate (per second)			
	10^{-4}	10^{-3}	10^{-2}	10^{-1}
P1-1	9836.38	11957.75	15553	13650
	12635.44	14809.87	17068.3	16640.25
	-	15126.7	-	-
P1-2	13778.49	14637.65	13393.14	14246.86
	13774.69	14540.15	14641.2	14334.07
	15494.53	13909.09	15352.93	15479.9
P1-3	14727.87	13268.9	15242.66	10474.66
	13345.99	14327.15	13446.59	9069.89
	16400.45	13208.73	14734.29	9369.29
	-	-	-	14455.66
P1-4	8559.832	11906.13	14878.87	13880.11
	13126.44	9571.481	10328.64	14869.68
	15597.1	16719.07	13798.85	13486.8
P1-5	9270.041	9804.404	11153.57	17856.72
	8452.764	7941.708	11247.49	-
	10033.83	15151.42	9295.067	-
P1-6	12290.9	14143.73	11521.91	16399.57
	11490.1	18250.91	15281.33	15640.67
	11633.16	13703.73	12161.35	15338.51
P1-7	11065.64	15918.8	14453.83	13007.01
	14183.23	14077.91	7474.738	15735.22
	11416.83	12264.07	13958.43	13399.1
P1-8	8824.121	10535.16	12130.81	13699.8
	13698.97	12148.15	19079.94	13775.61
	14881.33	18084.15	12711.32	18486.08
P1-9	17018.15	14324.9	13417.67	16425.5
	16862.87	15336.1	16742.92	18029.76
	15996.48	16991.01	14741.74	13893.48
P1-10	14047.95	13734.51	15782.55	13980.42
	16021.38	17116.04	18153.53	15285.29
	14020.17	15772.18	14291.03	14271.22
P1-11	13797.6	12742.85	13031.14	15713.74
	15040.37	13781	13710.62	15411.6
	15183.93	15537.65	16720.9	17188.7

Batch	Compressive Strength (psi)			
	Strain Rate (per second)			
	10^{-4}	10^{-3}	10^{-2}	10^{-1}
P1-12	12734.17	14562.63	12671.18	15127.61
	11893.9	13580.33	12925.05	14789.67
	10542.16	13895.5	14955.68	15575.14
P1-13	15059.15	13848.9	11850.71	17244.12
	14524.68	11883.16	14066.88	15400.2
	15051.71	13494.51	15281.49	13799.03
P1-14	8670.793	12394.95	7064.026	11561.63
	11750.97	9498.994	10800.79	10255.79
	12084.11	7328.227	9737.55	9341.779
P1-15	12951.32	14619.56	15819.23	18053.52
	13400.45	11069.71	15476.59	14149.42
	11801	12448.11	12844.96	12822.79

APPENDIX C. IMPACT TEST RESULTS FOR PHASE 1

Batch	v_{impact} = 16.73 fps			v_{impact} = 10.83 fps		
	Width (in)	Length (in)	Energy (ft-lbs)	Width (in)	Length (in)	Energy (ft-lbs)
P1-1	0.5094	1.0236	5.6210	0.5087	1.0169	2.4775
P1-1	0.5067	1.0157	2.2474	0.4606	1.0358	3.1686
P1-1	0.4925	1.0197	5.3289	0.4835	1.0319	4.5102
P1-1	0.4976	1.0055	5.1017	0.4677	1.0256	3.6782
P1-1	0.5079	1.0114	2.8374	0.5067	1.0413	5.0103
P1-1	0.5031	1.0240	3.1361	0.4929	1.0299	3.5514
P1-1	0.5055	1.0161	5.2920	0.4843	0.6378	2.2459
P1-1	0.5173	1.0228	4.2919	0.4941	1.0201	2.5549
P1-1	0.5055	1.0209	4.3140	0.5181	1.0240	3.0417
P1-1	-	-	-	0.4827	1.0280	3.8051
P1-2	0.5122	1.0264	9.4113	0.5138	1.0386	6.2508
P1-2	0.5165	1.0232	7.4346	0.5118	1.0539	6.5178
P1-2	0.5173	1.0457	9.4629	0.5248	1.0382	7.1440
P1-2	0.5213	1.0335	7.9288	0.4984	1.0539	7.9067
P1-2	0.5177	1.0437	11.4101	0.5197	1.0323	5.8113
P1-2	0.5205	1.0319	11.1593	0.5146	1.0579	5.8113
P1-2	0.5087	1.0189	8.4230	0.5189	1.0319	3.9718
P1-3	0.5110	1.0610	4.6636	0.5130	1.0744	3.3906
P1-3	0.4961	1.0508	8.0542	0.5028	1.0701	4.0197
P1-3	0.4925	1.0437	4.0463	0.5102	1.0917	5.2205
P1-3	0.5382	1.0606	3.9806	0.5138	1.0677	6.2265
P1-3	0.5000	1.0520	1.7598	0.5126	1.0945	2.0851
P1-3	0.5102	1.0594	5.5900	0.5150	1.1008	2.1625
P1-3	0.5118	1.0634	7.4346	0.5079	1.0504	1.7746
P1-3	0.5232	1.0598	7.4420	0.5110	1.0760	4.8731
P1-3	0.4909	1.0748	3.2018	0.5122	1.0449	4.1982
P1-4	0.4969	1.0638	4.8089	0.4606	1.0457	2.6501
P1-4	0.5079	1.0441	5.2684	0.4689	1.0071	3.2888
P1-4	0.5102	1.0327	5.2463	0.4976	1.0217	2.9834
P1-4	0.5055	1.0508	2.6619	0.4807	1.0437	1.5164
P1-4	0.5102	1.0409	6.2958	0.4783	1.0138	3.5668
P1-4	0.4972	1.0457	6.0355	0.4815	1.0154	2.0593
P1-4	0.4563	1.0657	6.1085	0.4496	1.0224	1.1521
P1-4	0.4795	1.0457	3.9290	0.5008	1.0555	2.2746
P1-4	0.4776	1.0236	2.5143	0.4508	1.0276	2.8809
P1-5	0.4736	0.9882	4.9513	0.4996	1.0283	3.6952

Batch	v_{impact} = 16.73 fps			v_{impact} = 10.83 fps		
	Width (in)	Length (in)	Energy (ft-lbs)	Width (in)	Length (in)	Energy (ft-lbs)
P1-5	0.4780	1.0213	2.6611	0.5008	1.0169	2.0600
P1-5	0.5228	1.0146	1.7930	0.5122	1.0209	4.8745
P1-5	0.4772	1.0252	5.0191	0.4622	1.0169	3.4164
P1-5	0.5012	1.0075	4.5485	0.4673	1.0217	4.0234
P1-5	0.5055	0.9984	7.1426	0.4803	1.0224	4.3251
P1-5	0.4846	1.0228	5.1320	0.4713	1.0138	2.6774
P1-5	0.4870	0.9925	5.8378	0.5217	1.0039	4.1997
P1-5	0.4957	1.0079	4.8391	0.4579	1.0217	3.7461
P1-5	0.5083	1.0311	4.3524	0.4598	1.0213	4.0485
P1-6	0.5252	1.0169	5.8467	0.5098	1.0366	6.5658
P1-6	0.5295	1.0228	5.0759	0.5154	1.0362	3.4909
P1-6	0.5217	1.0335	4.6002	0.5047	1.0492	3.1619
P1-6	0.4933	1.0307	7.1049	0.5047	1.0299	5.6637
P1-6	0.5244	1.0315	6.4249	0.5185	1.0398	5.3193
P1-6	0.4945	1.0260	6.6735	0.5264	1.0342	4.5987
P1-6	0.5161	1.0240	4.0721	0.5205	1.0413	5.2942
P1-6	0.5039	1.0339	6.0539	0.5130	1.0480	4.6990
P1-6	0.5122	1.0413	6.5879	-	-	-
P1-7	0.5098	1.0331	3.3780	0.5067	1.0217	2.0593
P1-7	0.5228	1.0020	5.5450	0.5177	1.0067	1.3866
P1-7	0.5189	0.9953	6.7811	0.5252	1.0181	4.7484
P1-7	0.5185	1.0575	6.5053	0.5189	1.0244	5.6888
P1-7	0.5165	0.9906	6.1653	0.5264	1.0091	6.7590
P1-7	0.5169	1.0157	3.5263	0.5185	1.0280	4.9225
P1-7	0.5165	1.0362	4.4637	0.5201	1.0311	4.5242
P1-7	0.5154	1.0280	4.5751	0.5138	1.0047	5.8113
P1-7	0.5134	1.0343	4.5080	-	-	-
P1-7	0.5193	1.0126	6.8881	-	-	-
P1-8	0.5189	1.0185	7.3594	0.5047	1.0130	7.2340
P1-8	0.5173	1.0000	5.9352	0.5035	1.0118	3.2644
P1-8	0.5248	1.0205	5.2485	0.5114	1.0201	4.3605
P1-8	0.5094	1.0213	3.1641	0.5118	1.0114	6.9648
P1-8	0.5126	1.0323	5.1032	0.5098	1.0205	5.9093
P1-8	0.5134	1.0276	7.6190	0.5059	1.0181	7.3328
P1-8	0.5071	1.0244	5.6549	0.5075	1.0205	6.7273
P1-8	0.5059	1.0283	5.0855	-	-	-
P1-9	0.5189	1.0465	7.6411	0.5094	1.0232	6.0310
P1-9	0.5161	1.0323	9.4629	0.5138	1.0134	7.5526
P1-9	0.5138	1.0492	5.5354	0.5173	1.0291	5.4919

Batch	v_{impact} = 16.73 fps			v_{impact} = 10.83 fps		
	Width (in)	Length (in)	Energy (ft-lbs)	Width (in)	Length (in)	Energy (ft-lbs)
P1-9	0.5067	1.0264	6.5525	0.5130	1.0299	1.3342
P1-9	0.5126	1.0453	8.0984	0.5091	1.0264	9.1826
P1-9	0.5126	1.0240	6.9751	0.5122	1.0319	7.7370
P1-9	0.5020	1.0280	7.7592	0.5189	1.0130	5.3193
P1-9	0.5035	1.0252	7.5895	-	-	-
P1-10	0.5185	1.0276	6.3401	0.5098	1.0256	7.0194
P1-10	0.5181	1.0484	2.9458	0.5110	1.0291	4.9697
P1-10	0.5146	1.0232	8.9909	0.5228	1.0185	10.3037
P1-10	0.5118	1.0425	11.4543	0.5063	1.0264	9.5662
P1-10	0.4996	1.0256	7.1138	0.5154	1.0405	9.3818
P1-10	0.5130	1.0307	11.6314	0.5189	1.0366	7.2347
P1-10	0.5150	1.0370	9.9276	0.5217	1.0425	10.0677
P1-10	0.5091	1.0535	5.7205	0.5154	1.0492	6.6565
P1-10	0.5177	1.0228	9.3818	-	-	-
P1-11	0.5252	1.0260	10.6504	0.5134	1.0382	4.0942
P1-11	0.5035	1.0441	5.6586	0.5154	1.0299	7.2318
P1-11	0.5232	1.0394	9.1605	0.5205	1.0378	6.8003
P1-11	0.5055	1.0457	10.5176	0.5201	1.0319	7.8919
P1-11	0.5114	1.0358	9.6473	0.5248	1.0386	5.9278
P1-11	0.5280	1.0307	9.8170	0.5142	1.0362	7.5895
P1-11	0.5236	1.0264	7.5526	0.5201	1.0374	6.7288
P1-11	0.5134	1.0398	10.1415	0.5264	1.0291	6.2685
P1-11	0.5173	1.0264	10.7979	0.5091	1.0370	6.1741
P1-11	-	-		0.5161	1.0307	8.0837
P1-12	0.5213	1.0406	6.8342	0.5177	1.0429	7.9435
P1-12	0.5169	1.0252	6.6233	0.5118	1.0307	8.3713
P1-12	0.5362	1.0287	3.7682	0.5165	1.0362	6.4677
P1-12	0.5287	1.0307	5.0176	0.5130	1.0228	2.7777
P1-12	0.5177	1.0413	5.1489	0.5000	1.0311	4.3465
P1-12	0.5146	1.0406	6.9987	0.5122	1.0366	4.4217
P1-12	0.5106	1.0280	4.8775	0.5055	1.0236	4.4718
P1-12	0.5256	1.0614	6.1107	0.5150	1.0276	7.2347
P1-12	0.5161	1.0425	6.5761	0.5157	1.0291	4.9446
P1-12	0.5165	1.0327	8.2164	-	-	-
P1-13	0.5217	1.0394	2.6095	0.5173	1.0161	7.6116
P1-13	0.5185	1.0394	4.5456	0.5142	1.0492	4.5478
P1-13	0.5173	1.0205	5.0626	0.5075	1.0256	3.5668
P1-13	0.5024	1.0496	4.5013	0.5138	1.0280	4.5478
P1-13	0.5012	1.0327	4.8148	0.5035	1.0346	3.0336

Batch	v_{impact} = 16.73 fps			v_{impact} = 10.83 fps		
	Width (in)	Length (in)	Energy (ft-lbs)	Width (in)	Length (in)	Energy (ft-lbs)
P1-13	0.5146	1.0406	9.3670	0.5165	1.0358	3.3389
P1-13	0.5122	1.0236	6.5577	0.5067	1.0236	1.1779
P1-13	0.5154	1.0461	3.2504	0.5110	1.0575	4.0212
P1-14	0.5161	1.0287	5.7884	0.5122	1.0413	3.8951
P1-14	0.5169	1.0409	3.2549	0.4976	1.0531	2.1367
P1-14	0.5181	1.0287	4.5692	0.5130	1.0323	3.3131
P1-14	0.5087	1.0476	2.7592	0.5142	1.0654	2.6759
P1-14	0.4843	1.0268	5.3813	0.5079	1.0177	4.1215
P1-14	0.5067	1.0630	5.8120	0.5181	1.0240	3.4149
P1-14	0.5059	1.0236	3.7070	0.5165	1.0394	2.1109
P1-14	0.5213	1.0130	2.7858	0.5047	1.0398	2.4708
P1-14	0.5138	1.0016	5.5597	-	-	-
P1-15	0.5161	1.0197	8.0689	0.5110	0.9965	3.5934
P1-15	0.5193	1.0047	3.5499	0.5079	0.9535	6.5658
P1-15	0.5043	1.0370	6.1321	0.4984	0.9992	3.5934
P1-15	0.5146	1.0142	6.8969	0.5126	1.0008	3.0852
P1-15	0.5268	1.0343	6.7797	0.5150	1.0126	6.5658
P1-15	0.5094	1.0535	6.6860	0.5083	0.9354	3.8456
P1-15	0.5213	1.0039	6.3408	0.5126	1.0280	5.5900
P1-15	0.5232	1.0220	7.1617	0.5142	1.0012	4.4239
P1-15	0.5173	0.9976	3.9209	0.5087	0.9980	3.3397
P1-15	0.4984	0.9740	8.3271	-	-	-

APPENDIX D. COMPRESSIVE TEST RESULTS FOR PHASE 2

Sand Type	G40759 (Quartz)	G4095 (Quartz)	G7030 (Quartz)	G4010 (Quartz)	G4060 (Quartz)	NJ65 (Silica)	NJ60 (Silica)	NJ70 (Silica)
f'_c (psi)	8953.047	11510.91	12256.54	11585.12	12919	12575.25	12372.25	11587.75
	11020.27	14414.39	13910.48	12835.5	12041.25	11489.75	11757.5	10869
	13954.37	12845.77	12458.96	14322.5	10250	12367.25	11678	10682.5
C_u	1.72093	1.56757	2	2.10417	1.68889	1.93548	2.05882	1.891892

Batch	Compressive Strength (psi)			
	Strain Rate (per second)			
	10^{-4}	10^{-3}	10^{-2}	10^{-1}
P2-1 (Quartz)	11966.68	12872.45	14822.42	13234.17
	10952.91	13699.07	13363.34	13466.61
	11905.93	13876.76	10775.4	12667.29
P2-2 (Quartz)	13013.32	11657.84	11794.25	10881.5
	10746.71	10948.89	11681.5	11746.75
	12673.47	12351.88	12300.25	11076.75
P2-3 (Quartz)	13423.48	11356.25	16093.25	15356.75
	10147.79	11959.25	17950.75	14279.5
	14839.21	11718.75	14422.75	6961.25
P2-4 (Quartz)	14411.75	12580.93	12652.5	13432.75
	13800.77	15266.83	14128.5	13948
	13690.99	13790.22	11597	-
P2-1 (Silica)	16748.75	12381.39	12756.71	11914.8
	14066.15	12695.93	10130.71	11746.75
	14674.02	13117.95	13070.36	12312.26
P2-2 (Silica)	13917.93	11234	15352.5	12911.25
	12999.47	14411.33	16538.25	13151.25
	15805.27	11197.15	14152	16287.25
P2-3 (Silica)	15798.15	14449.82	13115	13016.75
	12983.86	12519.17	18441.75	12111.5
	13569.91	16006.97	15389.75	12814.25
P2-4 (Silica)	13896.2	15293.62	16511.5	13695
	14488.18	13606.48	15999	10972.25
	15471.26	15522.79	16685.5	12322.75

APPENDIX E. IMPACT TEST RESULTS FOR PHASE 2

Batch	Sand Type	v_{impact} = 16.73 fps			v_{impact} = 10.83 fps		
		Width (in)	Length (in)	Energy (ft-lbs)	Width (in)	Length (in)	Energy (ft-lbs)
P2-1	Quartz	0.49	0.69	3.90	0.50	0.72	4.94
P2-1	Quartz	0.49	0.68	3.90	0.47	0.71	3.44
P2-1	Quartz	0.50	0.68	5.11	0.49	0.70	2.99
P2-1	Quartz	0.47	0.70	3.78	0.46	0.70	3.41
P2-1	Quartz	0.47	0.74	5.06	0.47	0.73	3.87
P2-1	Quartz	0.51	0.71	4.68	0.53	0.76	3.71
P2-1	Quartz	0.46	0.74	4.93	0.52	0.73	4.39
P2-1	Quartz	0.47	0.69	5.82	0.51	0.73	3.46
P2-1	Quartz	0.49	0.69	3.90	0.47	0.73	3.54
P2-2	Quartz	0.77	0.50	4.51	0.69	0.52	5.01
P2-2	Quartz	0.49	0.70	4.57	0.76	0.50	6.35
P2-2	Quartz	0.75	0.52	6.30	0.50	0.71	5.33
P2-2	Quartz	0.72	0.54	4.40	0.50	0.73	4.84
P2-2	Quartz	0.76	0.49	6.20	0.76	0.50	3.14
P2-2	Quartz	0.73	0.49	4.44	0.50	0.71	3.62
P2-2	Quartz	0.51	0.70	6.58	0.49	0.71	3.95
P2-3	Quartz	0.73	0.49	2.43	0.50	0.71	2.23
P2-3	Quartz	0.73	0.50	4.94	0.75	0.54	2.76
P2-3	Quartz	0.50	0.76	3.66	0.76	0.50	2.33
P2-3	Quartz	0.77	0.49	6.24	0.50	0.74	4.67
P2-3	Quartz	0.76	0.49	6.51	0.77	0.51	1.89
P2-3	Quartz	0.73	0.49	3.31	0.73	0.51	4.69
P2-3	Quartz	0.73	0.49	4.46	0.76	0.53	2.91
P2-3	Quartz	-	-	-	0.77	0.52	5.72
P2-4	Quartz	0.48	0.71	4.69	0.49	0.73	4.72
P2-4	Quartz	0.51	0.74	4.48	0.51	0.72	5.31
P2-4	Quartz	0.74	0.47	4.04	0.70	0.49	4.28
P2-4	Quartz	0.51	0.73	4.42	0.51	0.71	4.20
P2-4	Quartz	0.71	0.49	5.14	0.72	0.49	5.36
P2-4	Quartz	0.52	0.70	6.46	0.49	0.70	3.52
P2-4	Quartz	0.50	0.72	6.30	0.50	0.74	5.13
P2-4	Quartz	0.49	0.76	4.73	0.51	0.74	3.19
P2-1	Silica	0.52	0.73	6.23	0.50	0.69	3.87
P2-1	Silica	0.52	0.74	6.13	0.51	0.70	4.97
P2-1	Silica	0.51	0.71	5.67	0.49	0.70	4.97
P2-1	Silica	0.53	0.74	5.37	0.52	0.74	2.23

Batch	Sand Type	v_{impact} = 16.73 fps			v_{impact} = 10.83 fps		
		Width (in)	Length (in)	Energy (ft-lbs)	Width (in)	Length (in)	Energy (ft-lbs)
P2-1	Silica	0.51	0.73	5.51	0.48	0.70	4.42
P2-1	Silica	0.51	0.74	6.30	0.54	0.72	3.14
P2-1	Silica	-	-	-	0.50	0.71	4.12
P2-2	Silica	0.76	0.50	5.01	0.49	0.74	3.35
P2-2	Silica	0.49	0.75	3.35	0.74	0.50	4.02
P2-2	Silica	0.75	0.51	2.81	0.48	0.75	4.15
P2-2	Silica	0.53	0.72	4.95	0.73	0.49	4.12
P2-2	Silica	0.73	0.49	4.28	0.49	0.71	3.75
P2-2	Silica	0.49	0.72	4.67	0.53	0.72	4.92
P2-2	Silica	0.76	0.49	3.42	-	-	-
P2-2	Silica	0.50	0.71	6.32	-	-	-
P2-2	Silica	0.47	0.72	2.49	-	-	-
P2-2	Silica	0.73	0.49	3.79	-	-	-
P2-3	Silica	0.73	0.48	3.18	0.70	0.49	2.36
P2-3	Silica	0.77	0.47	3.07	0.48	0.77	2.02
P2-3	Silica	0.79	0.46	3.31	0.75	0.52	3.52
P2-3	Silica	0.74	0.50	2.71	0.48	0.70	2.05
P2-3	Silica	0.72	0.50	2.25	0.73	0.50	2.64
P2-3	Silica	0.49	0.72	2.43	0.75	0.50	3.85
P2-3	Silica	0.72	0.49	3.33	0.51	0.73	2.20
P2-3	Silica	0.53	0.75	3.42	0.49	0.73	2.81
P2-3	Silica	0.72	0.48	3.73	-	-	-
P2-3	Silica	0.73	0.48	3.18	-	-	-
P2-4	Silica	0.77	0.48	4.02	0.69	0.48	4.20
P2-4	Silica	0.73	0.52	4.85	0.50	0.68	5.04
P2-4	Silica	0.49	0.72	4.71	0.75	0.49	6.04
P2-4	Silica	0.72	0.49	3.71	0.51	0.73	3.44
P2-4	Silica	0.48	0.72	4.31	0.71	0.48	3.49
P2-4	Silica	0.74	0.49	6.02	0.52	0.72	3.22
P2-4	Silica	0.52	0.74	7.58	0.76	0.50	3.34
P2-4	Silica	-	-	-	0.48	0.74	3.62
P2-4	Silica	-	-	-	0.73	0.49	6.04
P2-4	Silica	-	-	-	0.69	0.48	4.20